

## **A porohyperelastic lubrication model for articular cartilage in the natural synovial joint**

G. N. de Boer<sup>1</sup>, N. Raske<sup>2</sup>, S. Soltanahmadi<sup>1</sup>, D. Dowson<sup>1</sup>, M. G. Bryant<sup>1</sup>, R. W. Hewson<sup>2</sup>

<sup>1</sup> School of Mechanical Engineering, University of Leeds, Leeds, LS2 9JT, UK.

<sup>2</sup> Department of Aeronautics, Imperial College London, London, SW7 2AZ, UK.

### **Abstract**

This work focuses on the proposed mechanisms for the lubrication of synovial joints and applies them to an idealised bearing geometry considering a porohyperelastic material (cartilage) rotating against a stationary rigid impermeable surface. The model captures the behaviour of all lubrication regimes including fluid film formation and boundary contact as the load capacity is increased, representing a major advancement in modelling cartilage mechanics. Transient responses in the fluid phase are shown to be faster than those in the solid phase with the former decaying over time as fluid is exuded from the material. The complex behaviour of fluid migrating to and from the lubricating film is captured which leads to a better understanding of the hydration and friction mechanisms observed.

Keywords: Poroelasticity; Lubrication; Finite Strain; Articular Cartilage.

### **1. Introduction**

Mammalian articular joints have evolved to allow for long term cyclic and shock loading. These joints are found at bone terminals and generally exhibit a large range of motion. The bone surface is covered in a relatively soft porous cartilage which is immersed and permeated with synovial fluid. This combination can more generally be described as a biphasic material with a deformable solid matrix structure and fluid-filled pores. This lubricating system has produced interfaces with remarkably low friction [1] and has garnered the attention of the tribology community for many years [2-4]. Under load the matrix structure deforms and the fluid plays an important role in the friction and load carrying capacity of the joint [5, 6]. When the cartilage layer is considered as a continuum the properties manifest as poroelastic or porohyperelastic whereby the porous matrix structure frustrates the free movement of fluid, increasing the interstitial pressure, and creates the primary load bearing component [7]. As the interstitial fluid is only restricted and not fully contained it drains from high pressure regions creating a stress-relaxation response where the initial load corresponds to an increase in stress followed by a decay. This behaviour has been recreated experimentally using compression and indentation tests [8, 9] the results of which have been used to derive material models. The process is complicated by the hierarchical cartilage structure causing the stress-relaxation profiles to change with compression depth [10, 11]. As the superficial tangential zone (the uppermost region of the cartilage forming the articular surface) tends to contain fibrils that are orientated along the plane of motion, while at the bone-fibril interface they are oriented normally. More recently researchers have turned to numerical methods to derive material properties and mechanical behaviour for a range of cartilage samples [12-14].

The primary function of the articular cartilage is to allow for a smooth articulation of the bone interfaces over prolonged periods of cyclic loading (e.g. walking). The mechanism that accomplishes this appears to be closely tied to how the friction manifests in the joint. Contacting porous media offer a combination of solid and fluid interactions, all of which can lead frictional phenomena. There is a strong correlation between load increases causing a reduction in coefficient of friction values [15, 16] indicating a higher loading of the fluid phase. This relation suggests that a pressurised interstitial fluid is desirable to support the applied load by minimising the load taken by the solid matrix.

It has been proposed that the relative solid-fluid load bearing capacity is driven by a migrating contact phenomenon between the two sliding surfaces [6, 17]. For a joint to maintain the interstitial pressurisation it must operate at a sufficiently high Peclet number, where the advective fluid transport, a pumping effect induced by the relative motion of the bearing surfaces, is large enough to mitigate the diffusive fluid migration from high to low pressure regions. Both the loading and movement trends extend beyond biological joints and appear to be a general phenomenon arising from poroelastic lubrication [18]. The realisation that the “pumping effect” is integral to poroelastic lubrication has spurred an interest in designing textured surfaces to improve joint replacement [19], as well as more general applications [20]. Recently the role of tribological rehydration, where fluid is drawn into the converging wedge and experiences very high pressure near the contact region which forces fluid from the bath into the porous medium, has been identified as a means of returning fluid to the porous medium after drainage [21-23].

Flow through a poroelastic media was initially described by Biot [24]. This has been expanded by researchers to increasingly describe articular cartilage [25-29]. The mechanics of biological tissues and soft poroelastic materials require a complex system of equations describing both the solid and fluid mechanics. To model this systems authors have often used the finite element method which is well suited to assembling and solving these equations and applying a variety of material specific constitutive equations. Large commercial finite element codes have been used to create high fidelity models of the biomechanics of a specific joint including the poroelastic cartilage layers [30-33]. These models are primarily concerned with understanding how the cartilage is loaded due to the geometry and motion of the joint. There have also been developments in creating finite element codes specifically built for biomechanics simulations and material characterisation [34]. There has been less attention focused on incorporating lubrication phenomena into these simulation [35, 36]. These phenomena are necessary to determine the operating friction and the fluxes across the porous boundary. This type of coupling between a porous interface and a lubricated boundary has already been utilised in the role of a lubrication film and how the generated pressures propagate into cracks within the solid bearing surface [37-39]. However, the significant difference here is the homogenised description of the porous domain as described by Darcy's equation.

This study describes a dynamic porohyperelastically lubricated system. This is achieved within the finite element software Comsol Multiphysics. We focus on the mechanical origins of soft porous flows and neglect physiological and electro-chemical effects. The solid components of the matrix of the porous material are described by hyperelastic governing equations which are coupled to the fluid components using a Darcy flow representation. Volumetric changes are therefore physically described by simultaneous solid displacements and fluid pressure changes. By assuming a hyperelastic solid phase the model can simulate the large deformations commonly experienced by articular cartilage or other soft materials, and when coupled with Darcy's equation these volumetric changes can also be due to fluid migration. The porous material is placed in lubricated contact with an impermeable wall. The interface describes lubrication across all regimes (hydrodynamic, mixed and boundary) using a combination of Reynolds equation and contact mechanics. This moves beyond models of the poroelastic lubrication regime alone [24-29, 35, 36], and allows a Stribeck analysis to be conducted for the porohyperelastic material. This reflects the nature of articulating joints which experience a range of lubricating conditions under normal operation [3]. In the case where lubrication is not considered the model derived reduces those where the poroelastic or porohyperelastic material properties of cartilage are investigated [30-34]. The model is demonstrated on a series of simplified cases and a realistic gait cycle highlighting the role of the solid and fluid in supporting applied loads and the friction each component experiences.

## 2. Materials and Methods

### 2.1 Problem Definition

In this article the porohyperelastic lubrication of articular cartilage rotating against a rigid impermeable surface is considered, allowing a simplified means of considering lubrication mechanisms encountered in a mammalian natural synovial joint and for direct comparison of data found in the literature. For this purpose a 2D cross-section through the contact was considered and the governing equations derived. The geometry is defined in the x-y plane in which the size of the body considered in the out-of-plane z direction is orders of magnitude larger than in either of the x or y directions. The contacting interfaces are assumed to be perfectly smooth, the material properties are isotropic and do not vary within the porous media.

Figure 1 shows the geometry where the body ABCD represents a converging-diverging wedge of cartilage, with outer and inner radii of  $R_0$  and  $R_1$  respectively, rotating at an axial speed of  $\Omega$  against a rigid impermeable surface EF. The boundaries AD and BC of the cartilage body extend far enough from the centre of the contact such that they do not influence the results generated and represent conditions in the remaining part of the cartilage (which is excluded from the model). A sector angle of  $\pm\theta$  was specified for the geometry and the domain is created with symmetry about the line  $x = 0$ . The cartilage forms a layer on the surface of a rigid body which itself is comprised of a solid material (bone). This is orders of magnitude stiffer than cartilage, such that the boundary CD is considered to be rigid and impermeable. The boundary AB represents the lubricated interface of cartilage against the rigid impermeable surface EF in fully flooded conditions. This forms a conventional line contact problem with additional constraints due to flow between the lubricating region and cartilage. The boundary AB is also in solid contact with EF. As such the mechanics of this must be included in the model, subsequently there is a transition from lubrication flow to no flow in the contacting region. The total load carried by the contacting interface L is the summation of fluid load due to pressure and solid load due to normal stress on AB. In order to generate this load, the boundary EF is deformed by an increment  $v_0$  in the surface normal direction, the variable  $v_0$  is known as the penetration depth of the contact.

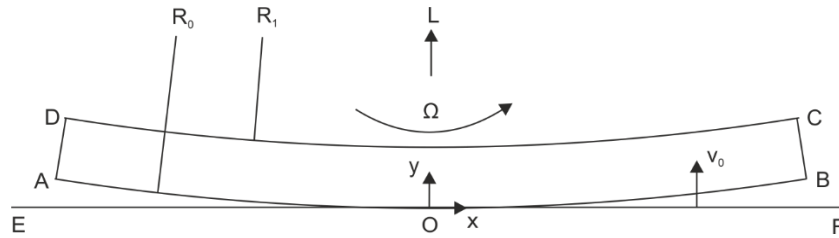


Figure 1 – Sketch of the poroelastic lubrication of the curved articular cartilage body against a flat rigid impermeable surface, in the case shown the penetration depth  $v_0 = 0$  and deformation of the contacting interface is not included.

## 2.2 Poroelastic Lubrication

In this model articular cartilage is considered to be biphasic in which the solid matrix of material deforms under load and a pressurised fluid interstitially fills the pores. The poroelastic description of cartilage is well-established in the literature as an accurate means of determining the behaviour of the material under load [22]. Poroelasticity is of particular concern to this model as the material undergoes significant deformation in the natural synovial joint which goes beyond the assumptions of infinitesimal strain theory (e.g. the deformations are of a similar magnitude to that of the material thickness). Models have been derived to capture this phenomenon [40-42] however these often neglect the lubricating pressure generated in a fully flooded contact and it is this functionality which the following model has been derived to capture. In the upcoming subsections the theory of poroelastic lubrication is outlined in which finite strain, porous flow and thin film flow theories are combined to form a mechanism which describes the functionality of the natural synovial joint.

### 2.2.1 Solid Mechanics

Deformation is considered by implementing finite strain theory to derive the constitutive equation for the solid phase of the poroelastic material. This is coupled to body forces generated due to the presence of a pressurised fluid. The model considers steady compression-sliding at the contacting interface and as such the effect of the body rotating is neglected in the solid phase and instead coupled to the fluid phase. Additionally, due to the 2D nature of the problem outlined plane strain assumptions apply. The equation of state for the solid phase is given by Eq. (1) which is derived from the conservation of energy of the solid phase in combination with a poroelastic coupling to the fluid phase. This formulation has been used by Simon [26] in previous studies investigating hyperelastic and poroelastic materials,

$$\rho_s \frac{\partial^2 \mathbf{u}}{\partial t^2} = \nabla \cdot (\mathbf{FS}) - \alpha \nabla p \quad (1)$$

where  $\mathbf{u}$  is the solid deformation,  $p$  is the fluid pressure,  $t$  is time,  $\rho_s$  is the drained solid density and  $\alpha$  is the Biot-Willis coefficient. The term  $\mathbf{F} = \mathbf{I} + \nabla \mathbf{u}$  is the deformation gradient tensor and  $\mathbf{S} = \frac{\partial W}{\partial \boldsymbol{\varepsilon}}$  is the 2<sup>nd</sup> Piola-Kirchhoff stress tensor. Where  $\mathbf{I}$  is the identity tensor,  $\boldsymbol{\varepsilon} = \frac{1}{2}(\mathbf{C} - \mathbf{I})$  is the strain tensor,  $\mathbf{C} = \mathbf{F}^T \mathbf{F}$  is the right Cauchy-Green deformation tensor, and  $W$  is the strain energy density. The Cauchy stress tensor is  $\boldsymbol{\sigma} = \mathbf{J}^{-1} \mathbf{FSF}^T$  in which  $\mathbf{J} = \det(\mathbf{F})$  is the volume ratio, the volume ratio relates to volumetric strain  $\varepsilon_{\text{vol}} = \mathbf{J} - 1$  of the solid and is used to couple changes in volume to the generation of pressure as described in Section 2.2.2. If the term related to pressure is neglected this formulation represents the behaviour of a hyperelastic solid material which is often used to describe the response of non-porous rubber-like behaviour under load.

In order to derive a suitable strain energy density for the solid phase two terms must be considered as described by Eq. (2),

$$W = \alpha W_{\text{iso}} + (1 - \alpha) W_{\text{vol}} \quad (2)$$

where  $W_{\text{iso}}$  is the isochoric strain energy density and  $W_{\text{vol}}$  is the volumetric strain energy density. The Biot-Willis coefficient  $\alpha$  varies between 0 and 1, with a value of 1 meaning that any change in volume of the solid directly produces a proportional change in the fluid phase. Previous studies have explored this case by neglecting the volumetric contribution to strain energy in Eq. (2) and only considering deformation as a process which occurs under isochoric conditions [36]. Here the strain energy density is not limited in this way and  $\alpha$  can take any value

between 0 and 1, implying that any change in volume leads to both changes in the fluid phase and volumetric compression/expansion of the solid material itself. In the case where  $\alpha$  approaches 0 all deformation occurs volumetrically and the fluid phase is not effected by volumetric strain, see Section 2.2.2.

As an example we use a metric to the most simple of hyperelastic solid models to produce representative strain energy densities for the porohyperelastic material. These can be replaced by any suitable definition so long as the constants used to describe the response can be obtained by physical testing. For the case specified here only the drained shear modulus  $G$  and drained bulk modulus  $K$  are required and both can readily be obtained for the drained solid phase. The terminology drained implies that these material properties are measured for the solid phase when the fluid has been entirely exuded. Based on the compressible Neo-Hookean hyperelastic model the isochoric and volumetric strain energy density functions are respectively described by Eqs. (3) and (4),

$$W_{\text{iso}} = \frac{G}{2} (\bar{I}_1 - 3) \quad (3)$$

$$W_{\text{vol}} = \frac{K}{2} (J - 1)^2 \quad (4)$$

where  $\bar{I}_1 = J^{-2/3} I_1$  is the 1<sup>st</sup> invariant of the isochoric part of the right Cauchy-Green deformation tensor and  $I_1 = \det(\mathbf{C})$  is the 1<sup>st</sup> invariant of the right Cauchy-Green deformation tensor.

### 2.2.2 Fluid Mechanics

The governing equation for pressure is described by conservation of mass in the fluid phase through the porous material, this is coupled to the total derivative of the volumetric strain in order to describe the porohyperelastic response. The conservation of mass for the fluid phase is given by Eq. (5), which describes the transient flow of fluid in a porous media coupled to changes of the solid phase [26],

$$\frac{\partial(\epsilon\rho_f)}{\partial t} + \nabla \cdot (\rho_f \mathbf{q}) = -\alpha\rho_f \frac{DJ}{Dt} \quad (5)$$

where  $\epsilon$  is the instantaneous porosity,  $\rho_f$  is the fluid density and  $\mathbf{q}$  is the fluid velocity. The fluid velocity is related to the pressure gradient by defining a permeability of the porous material  $\kappa$  and dynamic viscosity of the fluid  $\eta$ , such that we arrive at the viscous (or Darcy) definition of flow,  $\mathbf{q} = -\frac{\kappa}{\eta} \nabla p$ . In order to describe the porous flow response the fluid is considered to be linearly compressible such that  $\rho_f = \rho_0 \exp(\chi p)$ , where  $\rho_0$  is the density at ambient pressure and  $\chi$  is the fluid compressibility. The time derivative term in Eq. (5) is rewritten based on the drained porosity  $\epsilon_0$  and includes the effect of compressibility in both the fluid and solid phases. This leads to the definition of poroelastic storage  $S = \epsilon\chi = \epsilon_0\chi + \frac{(1-\alpha)(\alpha-\epsilon_0)}{K}$  which is a constant based on the fluid compressibility and solid bulk modulus (reciprocal of compressibility in the solid phase) specified, subsequently  $\frac{\partial(\epsilon\rho_f)}{\partial t} = \rho_f S \frac{\partial p}{\partial t}$ .

The Biot-Willis coefficient controls the proportion of the change in the fluid pressure due to volumetric changes in the solid. At a value of 1 all change in volume generates a proportionate change in the fluid pressure, whereas at a value between 0 and 1 the change in volume causes both some change in the fluid phase and some deformation of the solid structure as previously described. In Eq. (5) this change in volume is characterised by the total derivative of the volume ratio which includes rates of change in both time and space. This is subsequently expanded into two terms by Eq. (6),

$$\frac{DJ}{Dt} = \frac{\partial J}{\partial t} + \mathbf{v} \cdot \nabla J \quad (6)$$

where  $\mathbf{v} = \mathbf{v}_T + \mathbf{v}_R$  is the velocity of the body,  $\mathbf{v}_T$  is the translational velocity of the body, and  $\mathbf{v}_R = \boldsymbol{\Omega} \times (\mathbf{x} - \mathbf{x}_0)$  is the rotational velocity of the body. In this case the translation of the body is zero  $\mathbf{v}_T = 0$  and the rotation is defined by  $\boldsymbol{\Omega} = (0, 0, \Omega)$  as the axial velocity,  $\mathbf{x}$  is the position vector and  $\mathbf{x}_0 = (0, R_0, 0)$  is the location of the centre of rotation. Analyses into biphasic materials often neglect the 2<sup>nd</sup> term of Eq. (6) by removing the body velocity requirements, here we do not make such an assumption and include a generation of pressure in the fluid from the effect of the volume changing as the body rotates into and out of the contact. For general 3D body rotation, rather than the specific 2D case examined, the notation is exactly the same and the only difference is that all components of the axial speed and will be non-zero in value.

### 2.2.3 Boundary Conditions

Boundary conditions for each field variable, solid deformation and fluid pressure, need to be specified. These must physically represent the behaviour of the body rotating under load in which the porohyperelastic material is under steady compression-sliding at the contacting interface. Table 1 summarises the equations applicable for both  $\mathbf{u}$  and  $p$  on each of the boundaries defined in the model.

Table 1 – Boundary conditions for the porohyperelastic lubrication model of a natural synovial joint.

Boundary	Deformation, $\mathbf{u}$	Pressure, $p$
AB	$\mathbf{S} \cdot \mathbf{x}_n = -p_c \mathbf{x}_n$ $\mathbf{S} \cdot \mathbf{x}_t = \mu_s (\mathbf{S} \cdot \mathbf{x}_n)$	$p = p_{lub}$
BC	$\mathbf{u} \cdot \mathbf{x}_n = 0$	$\mathbf{q} \cdot \mathbf{x}_n = 0$
CD	$\mathbf{u} \cdot \mathbf{x}_n = 0$	$\mathbf{q} \cdot \mathbf{x}_n = 0$
AD	$\mathbf{u} \cdot \mathbf{x}_n = 0$	$\mathbf{q} \cdot \mathbf{x}_n = 0$
EF	$\mathbf{u} \cdot \mathbf{x}_n = v_0$	$\mathbf{q} \cdot \mathbf{x}_n = 0$

Deformation on each of the boundaries BC, CD and AD is constrained to zero in the surface normal direction  $\mathbf{x}_n$ , this represents the body rolling into and out of the contact as it rotates about the out-of-plane axis. The boundary AB is free to deform under load, in the contacting region where the porohyperelastic material cannot penetrate the rigid surface EF contact mechanics is applied. For this purpose a contact stress (denoted by a pressure term due to the physical significance of the boundary condition implementation)  $p_c$  is generated based on the amount by which the material must deform in order for there to be no penetration, this is subsequently applied to the boundary by constraining the solid stress contribution to this value in the surface normal direction. A force is generated in the surface tangential direction  $\mathbf{x}_t$  due to friction created by the bodies coming into contact. For this purpose, a coefficient of friction  $\mu_s$  is specified for the interface between the drained solid phase of the porohyperelastic material and the rigid impermeable surface under dry conditions. The rigid impermeable surface EF is deformed in the normal direction by an amount  $v_0$ , this variable known as the penetration depth is used to balance the load carrying capacity of the contact (see Section 2.2.5).

On AD, BC and CD the pressure boundary condition applied represents no flux through the surface, which is a zero surface normal gradient constraint. For CD this represents no flow through the material where it is connected to another rigid and impermeable surface that is not modelled here. For the boundaries BC and AD this condition implies that no fluid is transported beyond the edges of the annulus geometry defined. Pressure on AB is described by lubrication theory and the solution to the lubricating pressure  $p_{lub}$ , see Section 2.2.4 for details. The rigid impermeable surface EF is constrained to give zero flux generated through the surface, in the contact region between AB and EF this results in conditions consistent with a zero surface normal gradient for pressure. That is when the distance between the two surfaces is zero and there can be no flux from the thin film flow, therefore a switch from pressure calculated from the Dirichlet condition  $p = p_{lub}$  to the Neumann condition  $\mathbf{q} \cdot \mathbf{x}_n = 0$  occurs in this region.

### 2.2.4 Thin Film Flow

To describe the lubricating pressure generated in the fully flooded region between the surfaces AB and EF thin film flow theory is applied. The assumption invoked is that the radius of curvature of the body is far larger in size compared to that of the distance between the two surfaces, and as such the lubricated region can be treated as two nominally flat surfaces in relative motion. This is known as the Reynolds assumption and is subsequently used to neglect derivatives across the film thickness to derive an equation for the lubricating pressure in the direction of relative motion. Where the film thickness  $h$  is defined by the pointwise vertical  $y$ -distance between the two surfaces AB and EF (e.g.  $h = y_{AB} - y_{EF}$ ) and relative motion is aligned with the  $x$ -axis. In this model, fluid transport across AB due to flow from the lubricated region into the porohyperelastic material or vice versa is required. This is accounted for by an additional source term in the lubrication transport equation which describes the flow normal to that of relative motion.

The lubricating pressure is determined by the solution to Eqs. (7)-(8) on AB which describe the thin film flow on the boundary [5] with an additional term due flow into and out of the material,

$$\frac{\partial(\rho_f h)}{\partial t} + \frac{\partial(\rho_f Q)}{\partial x_t} = \rho_f V \quad (7)$$

$$Q = -\frac{h^3}{12\eta} \frac{\partial p_{\text{lub}}}{\partial x_t} + \frac{Uh}{2} \quad (8)$$

where  $Q$  is the volumetric flux (per unit depth) generated in the film and  $x_t$  is the  $x$  component of the tangential surface direction  $\mathbf{x}_t$ . The flow normal to the direction of relative motion is obtained from the fluid velocity acting on AB in the porohyperelastic material,  $V = \mathbf{q} \cdot \mathbf{x}_n$ , where a positive sign implies flow out of the rotating body. This assumes that the surface normal of AB and vertical axis are aligned and that the normal component of body rotation is negligible,  $\mathbf{v} \cdot \mathbf{x}_n = 0$ . The speed of relative motion is obtained from the body rotation on AB,  $U = \mathbf{v} \cdot \mathbf{x}_t$ , where a positive sign implies anticlockwise rotation and here  $U = \Omega R_0$ . Here the assumptions are that the tangential direction of AB and the horizontal axis are aligned and that the tangential flow component is negligible,  $\mathbf{q} \cdot \mathbf{x}_t = 0$ . It is also assumed that the rigid impermeable surface is at rest, the sliding motion of this surface can be included in the model cumulatively with the speed of relative motion  $U$  at the interface. Boundary conditions for  $p_{\text{lub}}$  are required which are consistent with Table 1 in order to solve for the field, and as such ambient pressure  $p_{\text{lub}} = 0$  is specified at both A and B. In 3D the equation for the lubricating pressure would also include derivatives due to flow in the out-of-plane direction which are neglected in the 2D case examined.

It is of note that the minimum film thickness  $h_{\text{min}} = \min(h)$  is always equal to zero  $h_{\text{min}} = 0$  when the two surfaces are in contact, however this does not necessarily correspond to a positive penetration depth  $v_0$  as a pressurised film is formed between the two surfaces and surface deformation subsequently occurs. Therefore  $h_{\text{min}}$  remains positive until the total load cannot be maintained by the film alone and contact of the two surfaces is onset. This also implies that the contact length  $b$  will become positive the instant that  $h_{\text{min}}$  is zero and that this does not correspond with the expected penetration length  $b_0$  of the contact (see Section 2.2.7).

The flow of fluid into and out of the porohyperelastic material is that acting normal to the direction of relative motion  $V$ . When there is a full fluid film present this term acts along the entire length of the body allowing fluid to flow over the interface throughout the film, when contact occurs this interfacial flow is zero and fluid can only travel into and out of the material on either side of the contacting region. The total mass flow in and out of the rotating body (per unit depth) can subsequently be derived by integrating this flow along the length of AB. This can further be partitioned into that acting to the left and right hand side of the contact leading to Eq. (9), Eq. (10), Eq. (11) and Eq. (12),

$$M_{\text{in},l} = - \int_0^{R_0\theta} \rho_f V \cdot H(-V) ds \quad (9)$$

$$M_{\text{in},r} = - \int_{R_0\theta}^{2R_0\theta} \rho_f V \cdot H(-V) ds \quad (10)$$

$$M_{\text{out},l} = \int_0^{R_0\theta} \rho_f V \cdot H(V) ds \quad (11)$$

$$M_{\text{out},r} = \int_{R_0\theta}^{2R_0\theta} \rho_f V \cdot H(V) ds \quad (12)$$

where  $s$  is the arc length of the undeformed boundary AB with  $s = 0, R_0\theta, 2R_0\theta$  occurring at locations A, O and B respectively.  $H(\cdot)$  is the Heaviside step function,  $M_{\text{in},l}$  is the mass flow per unit depth into the body on the left hand side of the contact,  $M_{\text{in},r}$  is the mass flow per unit depth into the body on the right hand side of the contact,  $M_{\text{out},l}$  is the mass flow per unit depth out of the body on the left hand side of the contact and  $M_{\text{out},r}$  is the mass flow per unit depth out of the body on the right hand side of the contact. These definitions facilitate an assessment of how fluid is flowing as the load and axial speed are varied over time. The total flow into the material is  $M_{\text{in}} = M_{\text{in},l} + M_{\text{in},r}$  and the total flow out of the material is  $M_{\text{out}} = M_{\text{out},l} + M_{\text{out},r}$ , noting sign convention the total flow on the left hand side is  $M_l = -M_{\text{in},l} + M_{\text{out},l}$  and the total flow on the right hand side is  $M_r = -M_{\text{in},r} + M_{\text{out},r}$ . The total flow on the boundary is therefore  $M = -M_{\text{in}} + M_{\text{out}} = M_l + M_r$ . In 3D each of these mass flow equations would become surface integrals representing the total mass flow on the contacting boundary.

### 2.2.5 Load Capacity

The total load capacity (per unit depth) for the contact  $L_t = L_s + L_f$  has contributions due to solid stress and fluid pressure acting on the porohyperelastic body while it is deformed. Each load contribution can be determined by integration on AB once the solutions to both deformation and pressure fields have been obtained. This results in Eqs. (13)-(14),

$$L_s = \int_0^{2R_0\theta} \|\mathbf{S} \cdot \mathbf{x}_n\| ds \quad (13)$$

$$L_f = \int_0^{2R_0\theta} p ds \quad (14)$$

where  $L_s$  is the solid load per unit depth and  $L_f$  is the fluid load per unit depth. The total load  $L_t$  varies monotonically with the surface normal displacement of the rigid impermeable surface EF (i.e. the penetration depth),  $v_0$ , therefore a relationship can be derived to satisfy a required operational load capacity for the contact  $L$ . This is defined by Eq. (15),

$$\frac{\partial v_0}{\partial t} = \lambda(L_t(v_0) - L) \quad (15)$$

where  $\lambda$  is chosen to be positive and constant. In the case where the operational load capacity  $L$  and axial speed  $\Omega$  vary with time the value of  $\lambda$  is chosen such the response generated by Eq. (15) is quasi-static and converges in a time period orders of magnitude smaller than any variance specified in the operational parameters. Therefore, at every measurable instance in time and for any steady-state solutions generated the total load and required operational load capacity are equal  $L_t(v_0) = L$ . This corresponds to a specific value of the penetration depth leading to a variation of this parameter over time depending on the operational conditions imposed. For the 3D case the integral functions of Eq. (13) and Eq. (14) become surface integrals including the geometry of the contact in the out-of-plane direction.

### 2.2.6 Coefficient of Friction

In Section 2.2.3 a coefficient of friction  $\mu_s$  was specified for the dry contact between the drained solid material and rigid impermeable surface. This differs to the coefficient of friction of the porohyperelastic contact  $\mu$  which also includes the influence of shear stresses in the fluid film. The porohyperelastic coefficient of friction is therefore determined by Eq. (16),

$$\mu = \frac{T_t}{L_t} = \frac{\mu_s + \mu_f \Gamma}{1 + \Gamma} \quad (16)$$

where  $T_t = T_s + T_f$  is the total tangential load,  $T_s = \mu_s L_s$  is the solid tangential load contribution,  $T_f = \mu_f L_f$  is the fluid tangential load contribution,  $\mu_f$  is the coefficient of friction due to fluid shear stresses, and  $\Gamma = \frac{L_f}{L_s}$  is the ratio of fluid to solid load acting along the boundary. The fluid tangential load  $T_f$  is given by integration of the fluid shear stress  $\tau$  acting along the surface of the body and  $\tau$  is itself obtained from thin film flow theory. This results in Eq. (17) and Eq. (18) respectively,

$$T_f = \int_0^{2R_0\theta} \tau ds \quad (17)$$

$$\tau = \frac{h}{2} \frac{\partial p}{\partial x_t} + \frac{U\eta}{h_\tau} \quad (18)$$

where  $h_\tau$  is the limited film thickness used only in the shear stress calculation and is subsequently described by Eq. (19),

$$h_\tau = h \cdot H(h - h_{\min,\tau}) + h_{\min,\tau} \cdot H(h_{\min,\tau} - h) + h_{\min,\tau} \cdot \delta(h - h_{\min,\tau}) \quad (19)$$

in which  $\delta(\cdot)$  is the Delta impulse function, and  $h_{\min,\tau}$  is a minimum film thickness used for the fluid shear stress calculation only. This approach is taken because in the case where  $h = 0$  the true fluid shear stress (e.g. where  $h_\tau = h$ ) becomes infinite. A maximum fluid shear stress  $\tau_{\max} = \frac{U\eta}{h_{\min,\tau}}$  is therefore obtained when the film thickness is zero  $h = 0$  and there is contact of the surfaces. When  $h \geq h_{\min,\tau}$  the true fluid shear stress is given and when  $h_{\min,\tau} < h \leq 0$  there is a transition from the true  $\tau$  to  $\tau_{\max}$ . Conventionally it is appropriate to select

$h_{\min,\tau}$  based on the size of surface asperities which have not been included in the current model. A number of other authors have used this assumption and proposed more complex solutions for problems investigating asperity contact in the mixed and boundary lubrication of elastic materials [43-45]. However, these models cannot be directly applied to materials also exhibiting a porous response and therefore the derived approach is based on a suitable assumption for measuring the fluid contribution to friction in this type of contact. In the 3D case the coefficient of friction is formulated in the same way but the shear stress calculation is determined as a surface integral over the lubricated boundary.

### 2.2.7 Contact Length

The penetration length is defined as  $b_0 = 2\sqrt{v_0(2R_0 - v_0)} \cdot H(v_0)$  which gives the length of the body as it penetrates the rigid surface when deformation of the interface is not considered, see Figure 2a. This subsequently allows an assessment how out of shape the contact length  $b$ , which includes deformation of the interface, becomes in comparison to the size of the penetration alone  $b_0$ . The contact length  $b$  is determined by Eq. (20),

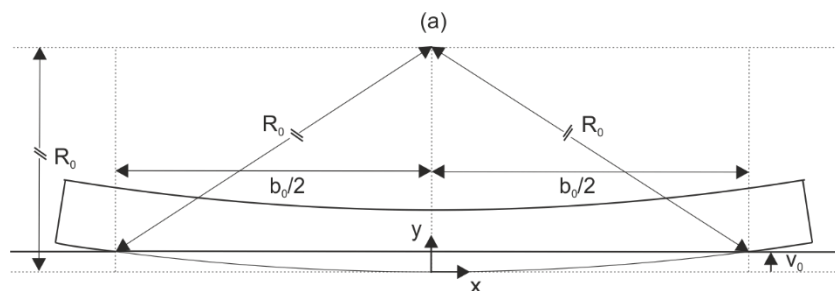
$$b = R_0 \sin(\theta_l) + R_0 \sin(\theta_r) \quad (20)$$

where  $\theta_l$  and  $\theta_r$  are the sector angles created by the contact region on the left hand side and right hand side of the vertical axis respectively. These can each be expressed in terms of the arc lengths within the contact region given on the left hand side and right hand side of the vertical axis,  $s_l$  and  $s_r$ , respectively. These are each in turn described by Eq. (21) and Eq. (22),

$$s_l = \int_0^{R_0\theta} \delta(h) ds = R_0\theta_l \quad (21)$$

$$s_r = \int_{R_0\theta}^{2R_0\theta} \delta(h) ds = R_0\theta_r \quad (22)$$

where integration over the arc length  $s$  of the Delta function of the film thickness  $\delta(h)$  on either side of the vertical axis defines the region in which the film thickness is zero  $h = 0$  and contact is onset. The contact length must be calculated using this approach because the region over which the film thickness is zero is not symmetrical about the vertical axis due to deformation of the interface under load, as shown in Figure 2b. When the penetration depth  $v_0$  is negative then both  $b$  and  $b_0$  are zero and the surfaces are not in contact, with  $h_{\min}$  taking a positive value. As  $v_0$  is decreased beyond zero then  $b_0$  is positive and  $b$  is zero, eventually the two surfaces contact such that  $h_{\min}$  is zero and  $b$  becomes positive. The latter two of these define the transition between full film lubrication including deformation and when the film can no longer support the load alone such that contact between the surfaces is onset. In the 3D case the penetration and contact length scales become the penetration and contact areas by considering integration in the out of plane direction that is negated in the 2D model.





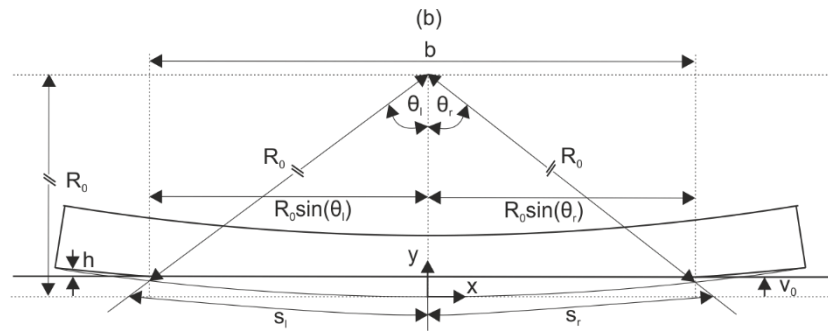


Figure 2 – Sketch of the porohyperelastic body in contact with the rigid impermeable surface showing geometric definitions of: (a) the penetration length  $b_0$  where deformation of the contacting interface is not considered; and (b) the contact length  $b$  where deformation of the contacting interface is considered.

### 2.3 Numerical Method

The problem was solved using Finite Elements (FE) as implemented in the software Comsol Multiphysics. The software facilitates complex coupling between the solid, fluid and thin film components of the model derived. Solutions are generated to investigate the effects of load and axial speed variation with time for a range of representative operating conditions.

#### 2.3.1 Discretisation

The domain ABCD was discretised using quadrilateral elements, this was achieved by distributing elements evenly along the lengths AB, BC, CD, AD with the same number given on AB/CD and BC/AD. It was found that grid independent results were achieved when the number of elements on AB/CD was 300 and on BC/AD was 30, giving a mesh with 9000 total elements. The rigid impermeable boundary EF required a single element (with no degrees of freedom). The porohyperelastic domain was discretised with 2D elements and 1D elements were applied to the lubricant domain. In each of these the governing equations were discretised by 2<sup>nd</sup> order polynomial shape functions.

#### 2.3.2 Solution Procedure

In order to solve the model numerically a series of initialisation steps were required to generate solutions under transient operating conditions. These steps were necessary to bring the initial solutions closer to that of the final required solutions, this is common practice in numerical modelling when solutions cannot be generated without a series of solution which evolve toward the final desired result. This approach was taken specifically to avoid initialisation from zero which would lead to a worse level of convergence, while these steps limit the modelling efficiency they are a needed requirement for the generating solutions. The steps required for this procedure are given in Table 2.

Table 2 – Initialisation steps for the porohyperelastic lubrication model.

Step	Lubrication	Load Capacity	Time Dependence
1	X	X	X
2	✓	X	X
3	✓	✓	X
4	✓	✓	✓

In Step 1 it was found that the problem was numerically sensitive to including the lubricating pressure from the outset, therefore the pressure boundary condition on AB is replaced in this step by a zero flux Neumann boundary condition,  $\mathbf{q} \cdot \mathbf{x}_n = 0$ . For the entire domain the deformation and pressure fields are initially set to zero and an arbitrary value for the deformation of the lower surface EF specified  $v_0$ , this value was chosen to allow contact and pressurised film formation between the two surfaces without the load balance requirement of Eq. (13) being satisfied. Steady-state conditions were applied such that the time derivatives in Eq. (1) and Eq. (5) were neglected.

Step 2 differs from the previous by the inclusion of the Dirichlet boundary condition for the lubricating pressure on AB and that the initial values for deformation and pressure were set to the result of Step 1. Steady-

state assumptions were applied to the solution of the lubricating pressure such that the time derivative term in Eq. (7) was neglected.

The load balance was then considered in Step 3, in which the initial values to deformation and pressure were specified from the result of Step 2. For this purpose, the deformation of the surface EF was allowed to vary with time as according to Eq. (15) until the load carrying capacity matched the required value. To achieve this in the software a time dependent solver was used and the total time in which the load balance converged was specified to be orders of magnitude smaller than any variation in the load defined transiently, see Section 2.3.3. For this purpose the value of the constant in Eq. (15) was set to  $\lambda = 1 \times 10^{-5}$  in all cases considered and the load balance converged in 0.01 s. The time derivatives in the governing equations were not included and as such the solutions calculated were quasi-static, all other conditions remain consistent with Step 2.

Time dependence was considered in Step 4, in which the initial values to deformation and pressure were given by the result of Step 3 for a specific load capacity under quasi-static conditions. In this step the time derivative terms of Eq. (1), Eq. (5) and Eq. (7) were included and various cases specified in which different variations in the load and axial speed with time were investigated, see Section 2.3.3. All other conditions remained consistent with Step 3.

### 2.3.3 Case Studies

Five different case studies were investigated in which a range of different variations in load and axial speed with time were considered. In each of these the material properties and geometry of the articular cartilage body were specified according to Table 3. This also includes values required in defining the operating conditions. It is of note from Table 3 that the geometry defined considers a 1 mm thick layer of articular cartilage rotating against a rigid impermeable surface under load. These values were chosen to best represent the material properties of articular cartilage and its operation in the natural synovial joint based on similar studies and experiments described in the literature [26, 36]. The value chosen for the solid-on-rigid coefficient of friction is  $\mu_s$  was selected based on experiments conducted considering dry cartilage against a hard metal surface under sliding conditions [2, 46]. It has been assumed by these authors that high friction in such contacts is due to exudation of water within the contact area and thus the best current value for ‘dry friction’, or in other words the solid coefficient of friction in drained conditions for a poroelastic material such as cartilage. The five different case studies considered are given in Table 4.

Table 3 – Material properties, geometrical parameters and operating conditions for the case studies investigated.

Name	Symbol	Value [Unit]
Oscillating frequency	f	1 [Hz]
Drained shear modulus	G	0.5 [MPa]
Minimum film thickness (shear stress)	$h_{\min, \tau}$	0.1 [ $\mu\text{m}$ ]
Drained bulk modulus	K	5 [MPa]
Steady-state load per unit depth	$L_0$	1.5, 0.3 [kN/m]
Outer radius	$R_0$	100 [mm]
Inner radius	$R_1$	99 [mm]
Poroelastic storage	S	2.08 [1/GPa]
Biot-Willis coefficient	$\alpha$	0.9
Drained porosity	$\epsilon_0$	0.8
Dynamic viscosity	$\eta$	0.001 [Pa.s]
Sector angle	$\theta$	$\pi/36$ [rad]
Permeability	$\kappa$	1 [ $\mu\text{m}^3/\text{mm}$ ]
Coefficient of friction (solid/rigid)	$\mu_s$	0.45
Fluid density at ambient pressure	$\rho_0$	1000 [ $\text{kg}/\text{m}^3$ ]
Solid density	$\rho_s$	1100 [ $\text{kg}/\text{m}^3$ ]
Fluid compressibility	$\chi$	0.1 [1/GPa]
Steady-state axial speed	$\Omega_0$	1 [rad/s]

Table 4 – Load and axial speed variation with respect to time for the case studies specified.

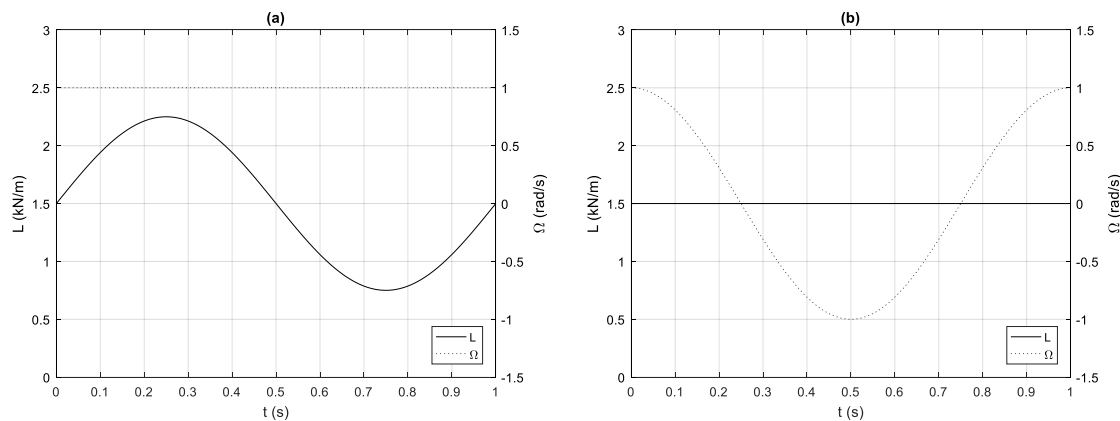
Case	Load Variation L	Axial Speed Variation $\Omega$
1	Constant	Constant
2	Sinusoidal	Constant
3	Constant	Sinusoidal
4	Sinusoidal	Sinusoidal
5	Gait cycle	Sinusoidal

Case 1 represents steady-state conditions for a given load capacity and axial speed, this means that because the operating conditions do not change that all derivatives with respect to time in the model are zero. In Case 2 the total load varies with time according to Eq. (23) and the axial speed is constant, this facilitates an analysis of the contact as the load is increased and decreased at constant speed. For Case 3 the axial speed varies with time as described by Eq. (24) and the load remains constant, this represents conditions under which the axial speed is increased and decreased for a given load. The load and axial speed both vary with time as given by Eq. (23) and Eq. (24) respectively in Case 4, this is representative of conditions where increases and decreases in both parameters can be studied. Case 5 represents a 2D metric to the gait cycle experienced during the operation of a natural synovial joint such as the hip [47]. In this case the axial speed is allowed to vary with time as according to Eq. (24), the load remains periodic over one period of oscillation in which there are two peaks and one trough in the first 60% of the cycle then remains constant for the second 40% of the cycle. In Eq. (23) and Eq. (24),  $f$  is the frequency of oscillation,  $L_0$  is the steady-state load and  $\Omega_0$  is the steady-state axial speed.

$$L = L_0 \left( 1 + \frac{1}{2} \sin(2\pi ft) \right) \quad (23)$$

$$\Omega = \Omega_0 \cos(2\pi ft) \quad (24)$$

For each of Cases 2-5 solutions were generated over 5 periods of oscillation, it was found that after 3 periods the results were periodic in time and as such only this data is presented in the remainder of the article. Figure 3a, Figure 3b, Figure 3c and Figure 3d respectively present the variation of load and axial speed with respect to time as described for Cases 2-5 and incorporates the values specified in Table 2 for the operational conditions. Case 1 is omitted because the values remain as those specified in Table 2. In Cases 1-4 the steady state load per unit depth is 1.5 kN/m and in Case 5 it is 0.3 kN/m which is based on values typically used to simulate wear in the hip joint [47].



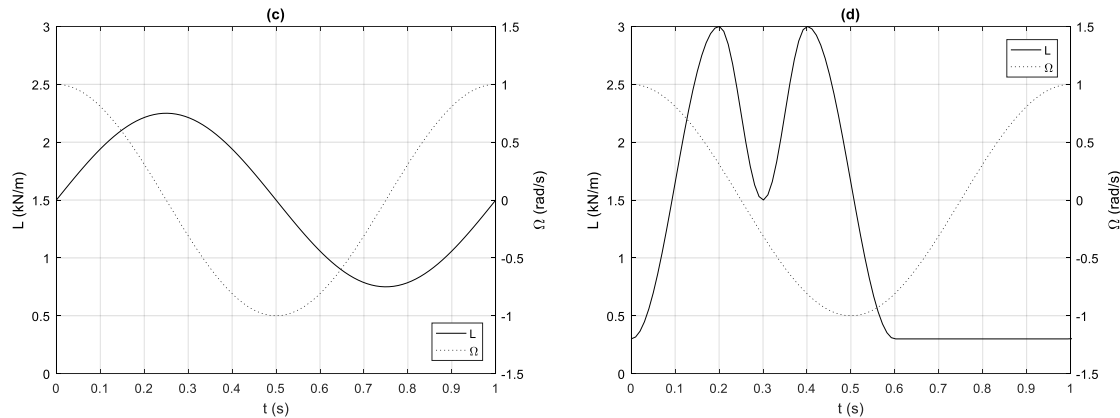


Figure 3 – Total load and axial speed variation with respect to time illustrating a period of oscillation at 1 Hz: (a) Case 2 – Sinusoidal load with constant rotation; (b) Case 3 – Constant load with oscillating rotation; (c) Case 4 - Oscillating load and rotation; (d) Case 5 – Gait cycle.

### 3. Results and Discussion

#### 3.1 Model Validation

To validate our computational framework, a simplified porohyperelastic tribological model was also implemented with the similar boundary and contact parameters as described by Graham, et al. [23] (see Appendix A). Our observations are in line with their results in terms of: i) contact pressures which are in the range of 150 – 200 kPa (although will be permeability dependant); and ii) that tribological processes contribute to the re-hydration of porous cartilage. We have further shown that tribological processes influence the hydration processes with the location of hydration similar to that hypothesised by Moore and Burris [21]. Our analysis has further shown that fluid flow in/out of the body occurs at multiple points across the tribological contact. Our Stribeck type analysis (see Section 3.2.2) also correlates well with that of Bonnevie, et al. [48] and Moore, et al. [49], which are similar in terms of the magnitude of coefficient of friction (boundary coefficient of friction  $\mu \sim 0.1 - 0.2$ , minimum coefficient of friction  $\mu \sim 0.01$ ) and lubrication transitions considering scaling factors associated with the use of the Sommerfeld number. In these experiments porous cartilage slides against a rigid impermeable surface and the lubricant used is a heavily viscous fluid ( $\sim 0.1 - 1$  Pa.s).

In addition to the comparison with literature as mentioned above the high permeability case for a column of porohyperelastic material was considered and compared to the well-established theory. This demonstrated that for the high permeability case that the resulting surface load and strains are in agreement with the stiffness of the solid material, as is the resulting volumetric change and fluid pressure field due to the pumping of fluid out of the domain.

#### 3.2 Steady-State Solutions

This section presents results relating to the steady-state operating conditions as described by Case 1. Firstly, data is given to show how stress and pressure are distributed in the material as well as how fluid flows across the contacting interface. Secondly, a Stribeck type analysis of the steady-state contact problem is conducted to analyse the effect of load and speed variation, this demonstrates how the coefficient of friction and contact length vary as the regime of lubrication is changed.

##### 3.2.1 Case 1: Constant Load and Axial Speed

Results are presented in this section for steady-state conditions described by Case 1 and were calculated using the solution procedure given in Section 2.3 (Steps 1-3). Figure 4 and Figure 5 respectively illustrate distributions of von Mises' stress and pressure in the material domain under load. Where the von Mises' stress is a measure of the magnitude of the Cauchy stress tensor (which includes both isochoric and volumetric stress). Higher values indicate that the solid phase is closer to its yield. The maximum value of the von Mises' stress and pressure are shown to be of a similar order of magnitude demonstrating a strong dependency between the two phases in this type of contact problem. It is also of note that the maximum fluid pressure occurs where the material is deformed the most on AB in the centre of the contact, whereas the maximum solid stress occurs in the centre of CD at the back of the cartilage layer. This indicates that at the poroelastic-rigid interface fluid pressure is generated, a phenomenon driven here by lubrication and contact mechanics, while the resulting deformation

results in a build-up of stress as the solid phase is compressed. At the extents of the domains BC/AD the solid deformation and fluid pressure are both shown to be zero such the material experiences no change in conditions, which is consistent with the body rotating into and out of the contact. On either side of the contact region the material undergoes both compression and tension and as such there is a change in the gradient of solid stress in the material in these regions. Due to the coupling between lubrication, rotation and volumetric strain this results in an asymmetric distribution of pressure along AB, in which there is a build-up of pressure as the material is deformed into the contact which then reaches a small negative value where the material is moving out of the interface.

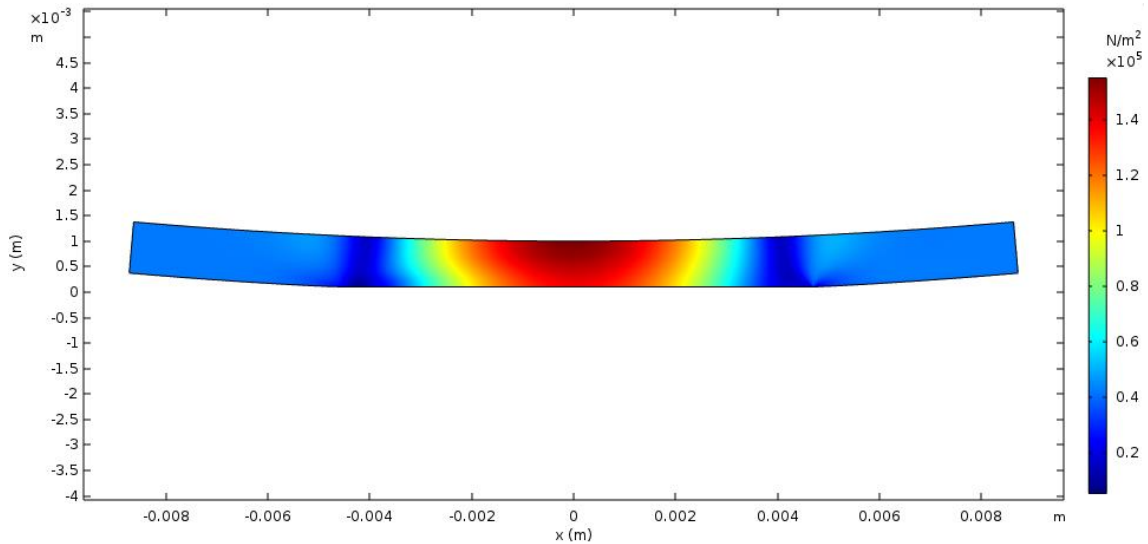


Figure 4 – Distribution of von Mises' stress in the solid phase for Case 1 (steady-state solution).

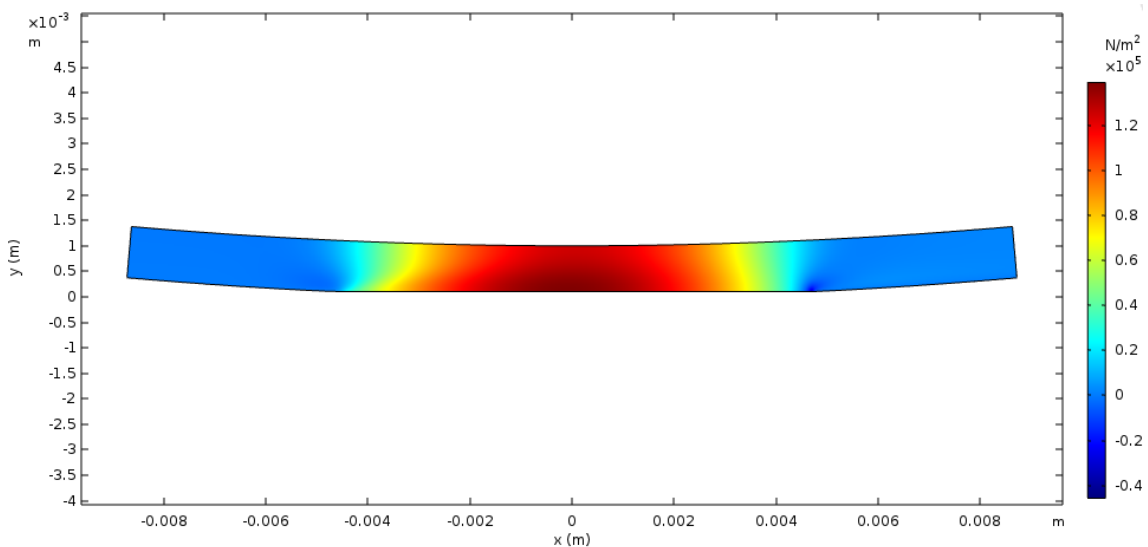


Figure 5 – Distribution of pressure in the fluid phase for Case 1 (steady-state solution).

The contact stress  $p_c$  and pressure  $p_{lub}$  on the interface AB are investigated in more detail in Figure 6a which shows distributions of these along the boundary length. Figure 6b shows distributions on the contacting interface of the lubricating flux and flow into and out of the body. Moving from left to right, as the body rotates into and out of the contact three regions are defined: (i) the inlet region where fluid is moving into the contact and there is no penetration of material; (ii) the contact region where there the film thickness zero, there is no lubricating flow and the material penetrates into the rigid impermeable surface; and (iii) the outlet region where fluid is moving out of the contact and there is no penetration.

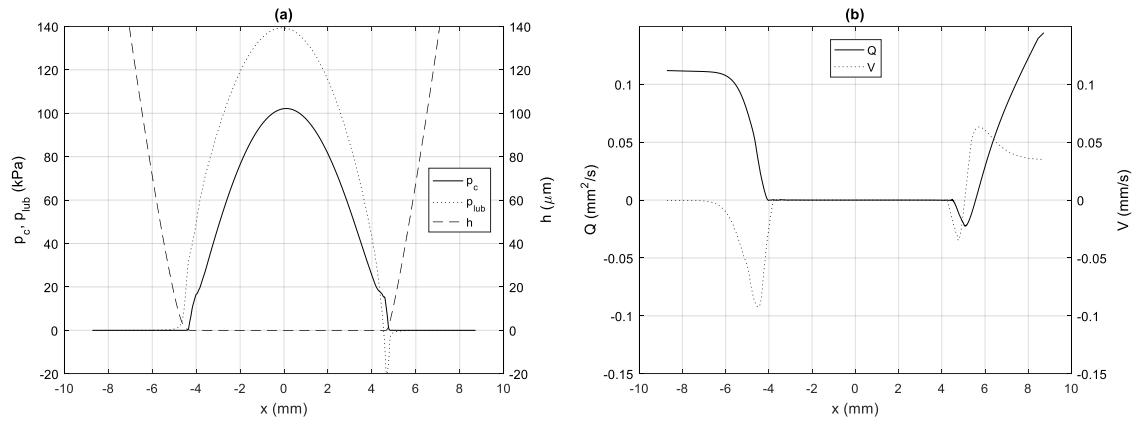


Figure 6 – Steady-state solution for the contacting interface AB in Case 1. Showing distributions of: (a) the contact stress,  $p_c$ , pressure,  $p_{lub}$ , and film thickness  $h$ ; and (b) the lubricating flux in the thin film,  $Q$ , and flow at the porohyperelastic surface,  $V = \mathbf{q} \cdot \mathbf{x}_n$ , where a positive sign indicates flow out of the rotating body.

In region (i) the contact stress is zero because there is no penetration (or contact) but the fluid pressure increases as the film thickness is reduced. The lubricating flux,  $Q$ , is initially positive (flow moving in the direction of body rotation) and near constant when the film thickness,  $h$ , is large but reduces to zero at the onset of contact. Corresponding to this the flow into the body,  $V$ , is initially zero when the film thickness is large but increases as the film thickness reduces, before returning to zero when contact is initiated.

Fluid pressure is initially larger than contact stress in region (ii) due to lubrication and no penetration in region (i). As material is deformed and solid stress generated, pressure is also built-up and maintains a larger value than the contact stress until the near outlet region, over the entire length of region (ii) the film thickness is zero. As the body rotates out of the contacting region the pressure is larger than solid stress and reduces at a faster rate along the boundary length to maintain the interface. This results in a negative pressure which subsequently changes the distribution of solid stress at the location where contact depreciates, and this leads to a difference in behaviour of the outlet region when compared to the inlet. There is no lubricating flux or flow into or out of the body in region (ii) because of the impermeable conditions imposed on the contacting interface EF and the fact that no fluid can flow through a gap of zero thickness.

In the outlet region (iii) pressure is initially negative at the location where contact no longer occurs and there is zero contact stress in the entire region due to no penetration. In the region far from the contact the film thickness is large and there is a positive lubricating flux with a corresponding flow out of the body. As the film thickness is reduced the lubricating flux is reduced and reversed flow is observed when the film thickness reaches a small enough value. Subsequently the flux returns to zero with film thickness at contact. Corresponding to this reduction in film thickness the flow out of the body is initially increased before reducing until flow into the body is observed where the flux is negative. This also subsequently returns to zero with the film thickness where contact occurs. Pressure in the outlet region is increased from the initial negative value to zero with increasing film thickness in the region. The negative pressure reached is significantly larger than that representing the saturated vapour pressure of the fluid ( $\sim -100$  kPa) and therefore cavitation does not occur.

The outlet demonstrates that to maintain the contacting interface there must be flow into the body before flow and can leave the body. This generates a negative pressure at the location where the surfaces separate and reversed flow in the lubricating film. It is observed around the outlet contact separation point there is a significant flow out of the body whereas around the inlet contact point there is no flow. This indicates that as the body initiates the contact fluid is drawn in, then there is no flow in the contact region and the fluid pressure and solid stress increase/decrease with penetration. At the outlet, to push enough fluid out as the body leaves the contact some more is drawn in from this region which generates reversed flow into the body and negative pressure. The movement of fluid into and out of the body as it deforms under load causes the instantaneous load carrying capacity of the fluid to be larger than that of the solid with  $L_f = 0.904$  kN/m and  $L_s = 0.596$  kN/m. The mechanism shown indicates that there is more flow leaving the body than entering it, with  $M_{out} = 0.219$  (g/m)/s and  $M_{in} = 0.185$  (g/m)/s. The system remains mass conservative in both the lubricating region and porohyperelastic material as according to the coupling between phases described in Section 2.2.

### 3.2.2 Stribeck Analysis

In order to conduct a Stribeck type analysis of the contact problem the penetration depth  $v_0$  was varied over a range of  $[-10 \mu\text{m}, 200 \mu\text{m}]$  and the computational procedure given in Section 2.3 did not include the load balance (Steps 1-2 only). For negative values of  $v_0$  a full fluid film is imposed initially and the penetration length  $b_0$  is zero. When  $v_0$  and therefore  $b_0$  become positive deformation of the interface restricts the minimum film thickness  $h_{\min}$  from reaching zero, as  $v_0$  is increased further contact occurs in which  $h_{\min}$  is zero and the contact length  $b$  is positive. It is of note that a penetration depth of  $v_0 = 200 \mu\text{m}$  represents a 20% strain of the material along the line  $x = 0$ , this is a significant compression and requires finite strain theory (rather than infinitesimal strain theory) to describe the solid phase response under high loads. Figure 7a shows the variation of the coefficient of friction  $\mu$ , the fluid coefficient of friction  $\mu_f$  and fluid-to-solid load ratio  $\Gamma$  versus the Sommerfeld number  $\frac{\eta U}{L}$ , and Figure 7b shows the variation of the contact length  $b$ , penetration length  $b_0$ , minimum film thickness  $h_{\min}$  and absolute value of the penetration depth  $|v_0|$  as a function of the Sommerfeld number. The Sommerfeld number is used to quantify variation in both load and speed as the penetration depth is varied over the imposed range.

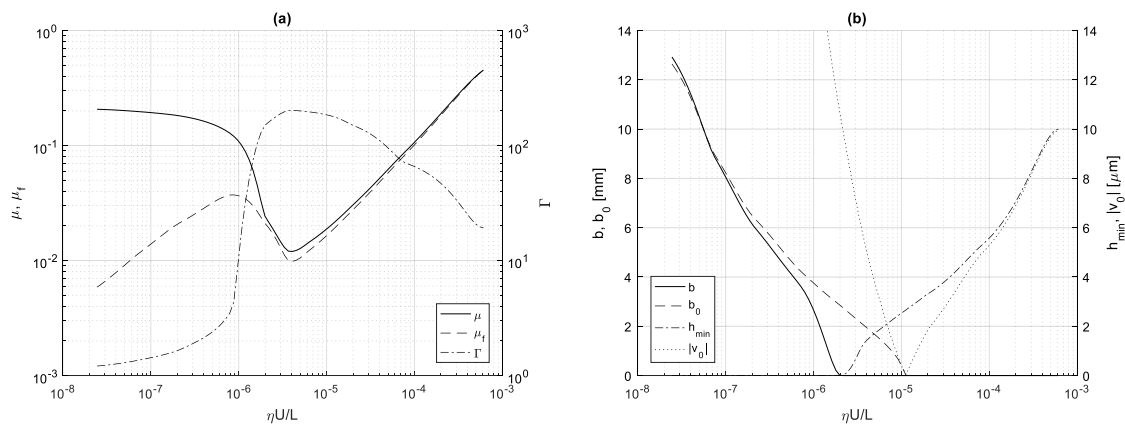


Figure 7 – Stribeck analysis of the contact showing variations in the following parameters a function of the Sommerfeld number  $\frac{\eta U}{L}$ : (a) The coefficient of friction  $\mu$ , the fluid coefficient of friction  $\mu_f$ , and the fluid-to-solid load ratio  $\Gamma$ ; (b) The contact length  $b$ , penetration length  $b_0$ , minimum film thickness  $h_{\min}$ , and absolute value of the penetration depth  $|v_0|$ .

Figure 7a demonstrates the different lubrication regimes which the system undergoes as the total load (or speed) is varied. This is only possible due to the inclusion of both the hyperelastic description of the solid material deformation combined with interstitial porous flow within the material, coupled to the lubrication between the porohyperelastic material and fluid film via Reynolds equation. At high values of the Sommerfeld number a full fluid film is formed between the two surfaces and no contact occurs, as the Sommerfeld number is reduced the fluid film thickness is also reduced and deformation of the interface is onset as an increased fluid pressure is generated. This causes the full film hydrodynamic regime to transition into an elastohydrodynamic regime, which is evidenced in Figure 7b where  $h_{\min}$  is positive. Where  $|v_0|$  and  $h_{\min}$  are similar in value there is negligible deformation and the lubrication regime is hydrodynamic. When  $|v_0|$  and  $h_{\min}$  differ (and  $h_{\min} \neq 0$ ) there is significant deformation of the interface due to fluid pressurisation invoking the elastohydrodynamic regime, where  $v_0$  is positive there would be penetration of the bodies if deformation was not considered and hence  $b_0$  is also positive in value. Further to this Figure 7a shows that in the hydrodynamic region the coefficient of friction has a linear negative gradient as is expected. Additionally, in these regimes the fluid coefficient of friction is the main contributor to the total coefficient and for which the fluid load is orders of magnitude larger than that of the solid (high values of  $\Gamma$ ).

As the Sommerfeld number is reduced further the fluid film cannot support the total load alone and contact is onset, in Figure 7b this is evidenced where  $h_{\min}$  becomes zero and  $b$  is positive. Note that this does not occur at the same instance as where  $v_0 = 0$  due to deformation of the interface. This also corresponds in Figure 7a to an increase in both the total coefficient of friction and fluid coefficient of friction but a reduction in the fluid to solid load ratio. In this region where the gradient of the coefficient of friction is large and positive this represents a transition to a mixed lubrication regime. In such a regime, surface asperities will be in contact and the gradient of this curve is likely to increase beyond that predicted here. However our approximation for calculating the fluid

tangential load is shown to be a good initial solution as the result is as expected for this type of lubrication regime. In the mixed regime Figure 7b shows that the size of the contact length is less than that predicted by the penetration length, indicating that the fluid film supports a significant proportion of the load.

When the Sommerfeld number is reduced beyond this region a boundary lubrication regime is reached in which the gradient of the coefficient of friction is small and positive in value, this corresponds to a reduction in both the fluid coefficient of friction and fluid to solid load ratio. In boundary lubrication the two surfaces are in direct contact and the solid response dominates the friction generated, this can be seen in Figure 7a where the fluid coefficient of friction is reducing since the film has less influence but the total coefficient of friction is still increasing. Figure 7b indicates that at very low Sommerfeld numbers the contact length will become larger than that expected due to penetration alone, which subsequently indicates an increase of the load supported at the interface by the solid rather than fluid film.

For reference the Sommerfeld number of the results presented in Section 3.2.1 is  $6.67 \times 10^{-8}$  and are therefore within the boundary lubrication regime, at this value the contribution the solid load is  $L_s = 0.59$  kN/m and fluid load is  $L_f = 0.91$  kN/m giving a ratio of  $\Gamma = 1.54$ . It is also of note that when either the mixed or boundary lubrication regimes are reached (and the contact length is positive in value) that there is no flow through the contacting region. This is because the film thickness is zero and no flow can occur between the non-existent gap, instead fluid flows into and out of the material in order to satisfy mass conservation over the entire domain.

### 3.3 Transient Solutions

Results in this section have been divided into Cases 2-5 to demonstrate the range of transient operating conditions considered. These were calculated using the solution procedure described in Section 2.3 (Steps 1-4). Each set of solutions presents the variation of fluid and solid load contributions and fluid flow into and out of the rotating body with respect to time. This facilitates an analysis of the poroelastic lubrication model in capturing the behaviour and mechanisms which underpin the operation of a natural synovial joints. It is of note that in each of the Cases presented contact of the surfaces is onset and the minimum film thickness is always zero throughout, boundary lubrication is expected under such conditions in the steady-state case and any variations observed from these results is related to the transient flow of fluid into and out of the material as the operational parameters are varied.

#### 3.3.1 Case 2: Sinusoidal Load and Constant Axial Speed

In Case 2 the body rotates in an anticlockwise direction with constant speed and the total load oscillates with respect to time. Figure 8a demonstrates that the fluid load is larger in magnitude than the solid load for the majority of each period and it exhibits a larger range of values. It is also observed that the solid load variation is slightly out of phase with the fluid load, responding more slowly to changes in the total load applied. This is linked to Figure 8b where the flow on the left- and right-hand-side of the body have significantly different responses across the surface AB. As the body oscillates from left to right there is a near constant flow into the body on the left-hand-side and near zero flow out of the body in this portion. On the right-hand-side when the fluid load is larger than the solid there is more flow out than into the body. Whereas when the solid load is larger than the fluid there is more flow in than out of the body. When the fluid and solid loads reach peak values so do the flow out of and into the body on the right-hand-side respectively. Additionally, when the fluid load is larger than the solid then the solid load is near constant and vice versa.

As the body rotates in an anticlockwise direction with constant speed and under load, fluid is drawn into the left-hand-side and pushed out of the right-hand-side. This is possible when the fluid load is larger than the solid and there is enough pressure generated in the fluid to cause fluid to flow under. This means when the total load is increased and decreased this causes a direct generation of fluid load. The solid load also varies but the response is slower and less in magnitude. Since the fluid load changes faster than the solid load, the fluid load becomes less than the solid while they are both decreasing, indicating that there is no longer enough fluid pressure to push fluid out of the body and as such fluid must be drawn into the body while the solid load is greater to maintain conservation of mass. Because the rotation is anticlockwise and the flow into and out of the body on the left-hand-side is near constant, the larger flow rate changes are on the right-hand-side. While this occurs the total solid load decreases and the fluid load then begins to increase as the body is pressurised by fluid influx. This process then becomes cyclic with the applied oscillating load.

Figure 8d shows that the contact length follows a similar trend to the load carried by the contact, where an increase or decrease in load causes the contact length to also increase or decrease. This implies that a larger load can be carried by a larger contact region. There is a slight phase difference between the penetration length and contact length which indicates that the size of the contact is controlled by the load variation and movement



of fluid within the contact region. Additionally, Figure 8c shows that the coefficient of friction has the opposite response. Where an increase or decrease in the load decreases or increases the coefficient of friction, which is exactly opposite to the trend demonstrated under steady-state conditions in the boundary lubrication regime. This shows the novelty in the transient responses presented, where the flow of fluid into and out of the body controls the magnitude of friction forces generated. Without this flow at the interface the behaviour of the system would be exactly described by the Stribeck type analysis and as given in Section 3.2.2, which alone does not describe the frictional responses observed over time as presented.

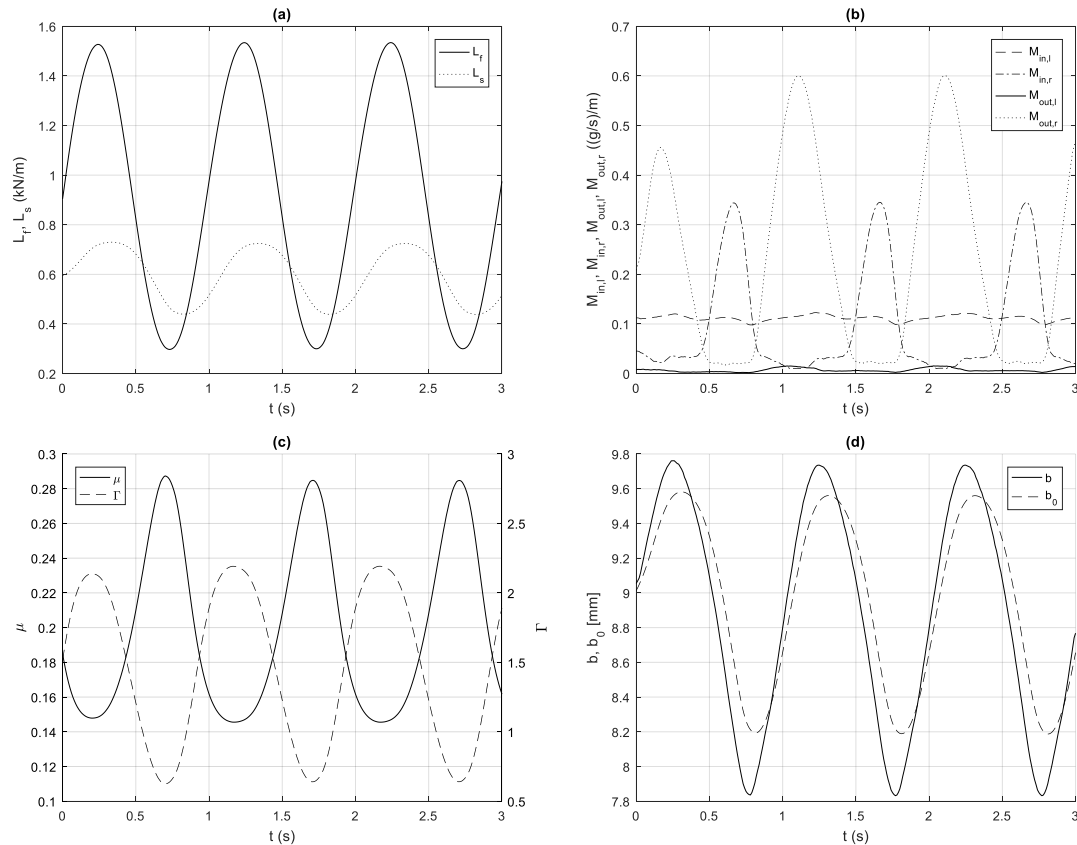


Figure 8 – Dynamic response for the body rotating anticlockwise at a constant speed with an oscillating load. Shown in (a) the fluid and solid load contributions; (b) the mass flow rates into and out of the porohyperelastic material at the upstream (left) and downstream (right) sides of the rotating body; (c) the coefficient of friction and fluid-to-solid load ratio; and (d) the contact length and penetration length.

### 3.3.2 Case 3: Constant Load and Sinusoidal Axial Speed

For Case 3 the total load is kept constant and the axial speed is sinusoidal with respect to time, with a maximum clockwise and minimum anticlockwise rotation achieved during each period of oscillation. It is shown in Figure 9a that as the axial speed is reduced from the maximum value to zero there is a reduction in fluid load and increase in solid load. These changes are of a similar order of magnitude such that the total load remains constant. As the axial speed continues to decrease to the minimum value the fluid load increases and the solid load decreases, this process then repeats as the axial speed oscillates. Subsequently each of fluid load peaks and solid load troughs correspond to maximum/minimum axial speeds, and each of the fluid load troughs and solid load peaks correspond to when the body is instantaneously at rest.

Figure 9b indicates that there are three repeating patterns in terms of fluid flow which correspond to this case. When the axial speed is positive (anticlockwise rotation) there is a similar instantaneous response as shown for the steady-state solution in Section 3.1. Fluid flows into the body on the left-hand-side and out of the body on the right-hand-side, to provide enough fluid for this there is an additional amount of flow into the right-hand-side and near zero out of the left-hand-side. However, as the axial speed tends to zero there is a corresponding reduction in all flow contributions expect flow into the left-hand-side (direction opposing positive rotation) which increases. When the axial speed becomes negative the flow into the left-hand-side is increases along with flow out of the right-hand-side and flow into the left-hand-side, the flow into the right-hand-side is near zero. This is the direct

opposite of the case when axial speed is positive, this periodicity can be seen in Figure 9b where there is similarity of the flow components  $M_{out,l}$  and  $M_{out,r}$ ;  $M_{in,l}$  and  $M_{in,r}$  when the axial speed oscillates.

The coefficient of friction is shown to vary in Figure 9c between 0.175 and 0.205 over the duration of one period, this is a significant difference given that the total load applied is constant. Corresponding to this variation the fluid to solid load ratio has the exact opposite trend, where any increase or decrease in friction directly produces a decrease or increase in the load ratio as was observed in Section 3.3.1. Figure 9d shows that there is also a significant variation in the contact length despite the load remaining constant. Interestingly, as the load applied is increased or decreased this generates an increase or decrease in both the coefficient of friction and contact length. Which is in contrast to the results presented in Section 3.3.1 where the coefficient of friction had the opposite response. This relates to the motion of fluid into and out of the material which is much lower in magnitude for Case 3 than for Case 2 since the total load is not changing and therefore less fluid needs to be transported through the material to maintain mass conservation.

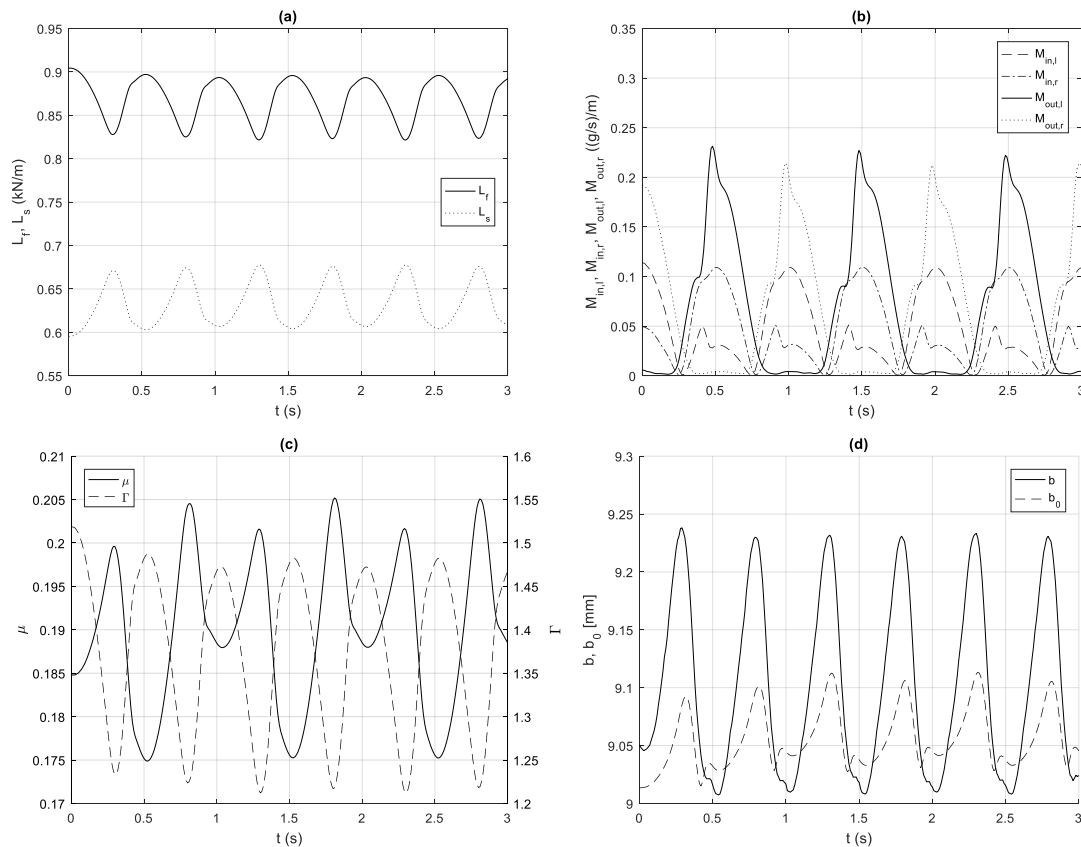


Figure 9 – Dynamic response for a body with oscillating rotation and a constant applied load showing: (a) the fluid and solid load contributions; (b) the mass flow in and out of the porohyperelastic material on the subscripted side of the contact region (left or right); (c) the coefficient of friction and fluid-to-solid load ratio; and (d) the contact length and penetration length. Note that the body is oscillating at 1 Hz and at  $t = 0$  the body is rotating anticlockwise at 1 rad/s; at  $t = 0.5$  the rotation has changed to -1 rad/s.

### 3.3.3 Case 4: Sinusoidal Load and Axial Speed

Case 4 considers sinusoidal variation of both total load and axial speed with respect to time, combining the oscillatory aspects of both Case 2 and Case 3. Figure 10a indicates that as the total load oscillates with time the fluid load responds in a similar manner, whereas within each period the solid load initially increases to a maximum but then decays (with some small deviations) to a minimum. This is in contrast to the behaviour exhibited in Case 2 where both the fluid and solid load contributions oscillated with the total load, this difference is caused by the variation in axial speed and is coupled to the flow into and out of the body.

Figure 10b shows that the response of the flow into and out of the body is complex but there are some observations which can be made. Flow out of the body on either side is largest when the fluid load is greater than the solid load, flow into the body on either side is largest when the solid load is greater than the fluid load. The flow into and out of the right-hand-side is largest when the axial speed is positive, flow into and out of the left-

hand-side is largest when the axial speed is negative. This behaviour shows the necessity in defining the lubricating film to provide the model with the capacity to predict such trends, the authors would like to propose a challenge to the readers to better understand these mechanisms and the use of a porohyperelastic model in describing the behaviour of such systems.

The variation of the coefficient of friction, fluid to solid load ratio, contact length and penetration given in Figure 10c and Figure 10d show similar responses and magnitudes to those presented for Case 2 in Section 3.3.1. However in each the maxima and minima are either flattened out or steepened. For example comparing the coefficient of friction in Figure 8c and Figure 10c over one period shows that the minimum value is reached in Case 3 with a smoother transition than for Case 1, whereas the maximum value is reached in Case 3 with a sharper transition than for Case 1. In Figure 10d the contact length is shown to be larger than the penetration length at higher loads and lower than the penetration length at lower loads, this suggests an expansion of the material as load is increased and a contraction of material as load is decreased. Corresponding to this, by inspecting Figure 10b it can be seen that when the material is expanding fluid is exhumed much more than absorbed and when the material is contracting that fluid is absorbed much more than it is exhumed.

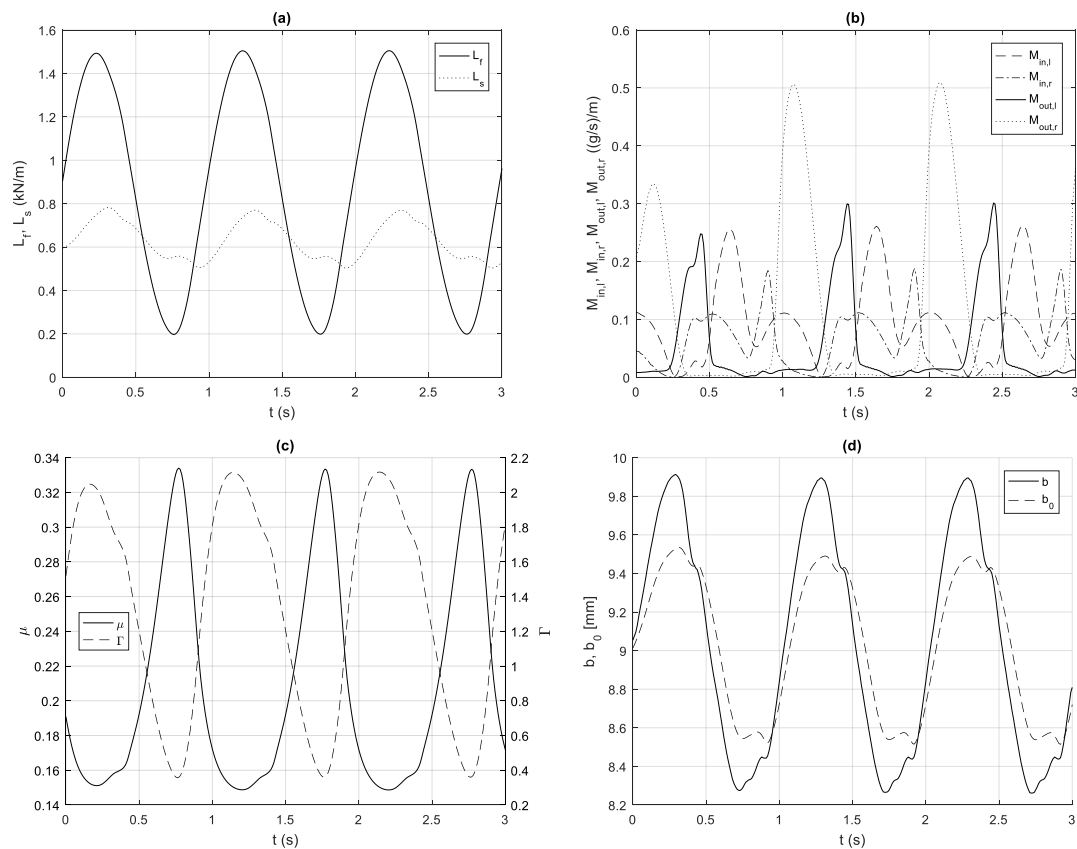


Figure 10 – Dynamic response for a body with oscillating rotation while experiencing an oscillating load: (a) the fluid and solid load contributions; (b) the mass flow in and out of the porohyperelastic material on the subscripted side of the contact region (left or right); (c) the coefficient of friction and fluid-to-solid load ratio; and (d) the contact length and penetration length. Note that the body is oscillating at 1 Hz and at  $t = 0$  the body is rotating anticlockwise at 1 rad/s; at  $t = 0.5$  the rotation has changed to -1 rad/s.

### 3.3.4 Case 5: Gait Cycle Loading and Sinusoidal Speed

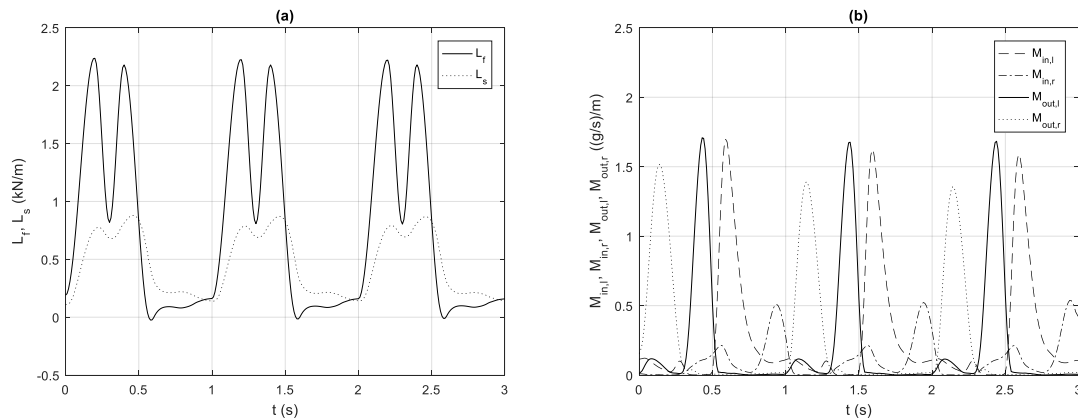
The total load varies according to a gait cycle type profile and the axial speed variation is sinusoidal in Case 5. Figure 11a demonstrates that during the first part of the cycle where the two peak total loads are achieved that there are also peak values of both the fluid and solid load contributions. Comparing the two peak values shows that the fluid load at the first is larger than at the second and vice versa for the solid load. Additionally, the range and rate of change of fluid load are larger than that of the solid load. This indicates how the solid load reacts more slowly than the fluid load to variation in the total load applied. During the part of the cycle where the total load is constant the solid load is greater than the fluid load, also as the total load remains constant the solid load reduces and the fluid load increases until they reach similar values at the end of the period. Figure 11a also shows that the

instantaneous fluid load can be negative in value, implying that pressure is applying suction at the interface to maintain contact. For all instances the negative pressures obtained are significantly larger than the vapour saturation pressure, as was reported in Section 3.2.1 and therefore cavitation does not occur.

Flow into and out of the body presented in Figure 11b and shows an interesting periodic pumping mechanism, peak values of each flow component are observed during the different stages of each cycle. Corresponding to the first peak in total load the flow out of the right-hand-side reaches a maximum and then decays to zero for the remainder of the period. During this time the rotation is anticlockwise and this is consistent with flow being exuded from the material when the fluid load is greater than that of the solid. During the second peak in total load the flow out of the left-hand-side reaches a maximum and then decays for the remainder of the period, in this time the rotation is clockwise and again this is consistent with fluid moving out of the body when the fluid load is greater than the solid load. Subsequently when the rotation is negative and the solid load is now greater than the fluid there is a peak flow in the left-hand-side, when the rotation becomes positive and the solid load remains greater than the solid there is a peak flow into the right-hand-side.

Figure 11c shows that the variation of the coefficient of friction is directly related to the fluid to solid load ratio as observed in all Cases reported. When the ratio is increasing (and the fluid becomes more load carrying) the coefficient of friction is decreased, and when the ratio is decreasing (and the solid becomes more load carrying) then the coefficient of friction is increased. This occurs regardless of the total load carried by the contact, such that over the first 60% of each period increases and decreases of the total load give rise to decreases and increases in the coefficient of friction. Whereas in the remaining 40% the total load is constant but significant changes in the proportion of load carried by the fluid and solid which results in both increases and decreases in the coefficient of friction.

This is supported by Figure 11b and Figure 11d which show that when the material expands and the contact length is greater than the penetration length fluid is exhumed into the lubricating film, whereas when the material contracts and the contact length is less than the penetration length that fluid is absorbed from the lubricating film. Fluid is exhumed mostly over the first 60% of each period and absorbed mostly over the remaining 40%, meaning that as fluid is exhumed from the material to the film the coefficient friction changes directly with the total load but when fluid is absorbed from the film to the material the coefficient of friction decreases as fluid is supplied and increases as the supply is reduced. Therefore a hydration mechanism is formed in which fluid flow across the interface changes the proportion of load carried by the two phases. Resulting in: an expansion and contraction of the material as fluid moves into and out of the interface; and an increase or decrease in the coefficient of friction when the fluid or solid carries more load than that of the solid or fluid respectively.



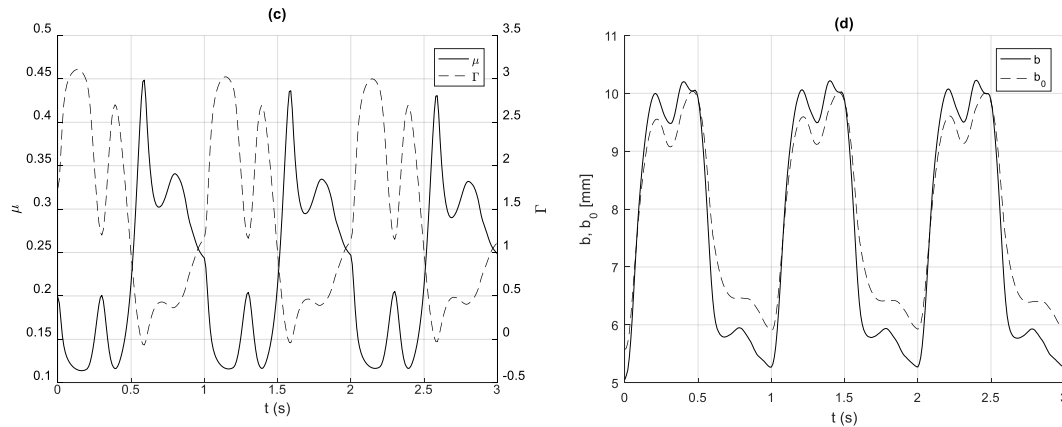


Figure 11 – Dynamic response for a gait cycle showing: (a) the fluid and solid load contributions; (b) the mass flow in and out of the porohyperelastic material on the subscribed side of the contact region (left or right); (c) the coefficient of friction and fluid-to-solid load ratio; and (d) the contact length and penetration length.

#### 4. Summary and Conclusions

Lubricating porous media, such as natural synovial joints, may deform in such a way that they can accommodate a range of loads and motion. While the motions can be steady state in man-made bearings, they are often oscillatory and dynamic in biological systems. The resulting deformations may be of a similar magnitude to the material thickness [43]. To simulate a complex process of this nature one must couple a system of mathematical equations describing:

- the solid mechanics accounting for large strains experienced under dynamic loading;
- the time dependant fluid flow within the porous media;
- the thin film lubricating flow that forms between the interfaces;
- and contact mechanics for the region where the thin film does not form.

Here a dynamic hyperelastic model is used to describe the deforming solid matrix. Previous studies have also used hyperelastic representations of porous materials [22, 40–42]. The fluid flow is described using a time dependant conservation equation which adopts a Darcy representation of flow in the porous media [50]. These are coupled using source terms to create a porohyperelastic material. Reynolds equation is used determine the pressure distribution at the lubricating boundary, an approach commonly found in the study of man-made bearings [51]. Where the film does not form, contact is assumed such that there is a zero-flux condition. The addition of this boundary representation allows for the simulation of bearings for mechanical purposes and for simple representations of articulating joints, noting that the case of two contacting porous materials (as is the case in natural articulating joints) requires further development of this boundary condition. However, cartilage moving against an impermeable boundary is commonly found in experimental studies [52].

The results from Cases 4 and 5 are analogous to the migrating contact phenomena present in articulated joints [6, 51]. When the joint is under oscillating motion the pressure contribution from the fluid and solid follow two different profiles with the fluid pressure reacting faster to changes in speed and direction. This corresponds to complex fluxes at the porous material boundaries. The resulting interaction produces a rehydration process similar to that proposed in [53, 54] whereby fluid is forced into the porous body at the downstream contact point. However, along most of the boundary fluid is secreted into the thin film. Mass is conserved in the system by accounting for the rotating bearing, which is saturated, and is forced out due to the compression. The process is strongly dependent on the direction of rotation and the boundary fluxes oscillate accordingly. The load support mechanism also appears to be dominated by the state of the fluid pressure rather than solid stress, which exhibits similar directional changes (though they are delayed) but much smaller changes in magnitude. The fluid response falls into line with experimental studies that have found increased fluid load fractions with increased deformation rates [55]. This goes to support the evidence presented showing that a dynamic contact exhibits significantly different friction and load responses in comparison to a static contact under the same compression and sliding conditions due to the flow of fluid across the interface.

Steady-state simulations also showed that the contact stresses are of the expected order of magnitude to experiments published in the literature [23] and that the hydration occurs at the same locations as observed by Moore and Burris [21]. The Stribeck analysis conducted also produced a minimum coefficient of friction of ~

0.01 and boundary coefficient of  $\sim 0.1 - 0.2$  which correlate well with the experiments published [48, 49]. This also showed how the model is capable of modelling the entire range of lubrication regimes from a full fluid film through to boundary contact. Surface asperities were neglected in the formulation and it remains future work to include topological effects in the model of porous-elastic lubrication.

An important consideration to make is that three-dimensional geometries must also be considered to accurately represent natural synovial joints, the model derived in this paper can be applied to such problems and the behaviour under load concurrently described. It is likely that the phenomena observed in this work would extend to impulse loads, where the fluid absorbs a major component of the applied load compared to that of the solid and subsequently dissipates over time, creating a damping effect in the joint. It is envisaged that this type of analysis will be furthered to deliver a means of analysing the modes and location of damage in natural joints. The authors also highlight the need to reduce the number of initialisation steps required in the solution procedure derived, this will improve computational efficiency and ease of use for the model in general.

Further development is required to address the physiological and electro-chemical phenomenon that arise in natural joints. A fully predictive model requires a coupling of the interactions that arise from both biological and mechanical systems and should be established concurrently with the development of the basic mechanisms as undertaken in the present article. Osmotic pressures and the corresponding hydration lubrication mechanism would require significantly larger timescales than investigated thus far. Viscoelasticity of the solid phase would also not be observed until larger timescales are considered. The shear-thinning dependency of synovial fluid, geometrical variations, anisotropy and cross-dependency of material properties will have more significant roles under the current timescales.

### Acknowledgements

The authors acknowledge the Leverhulme Trust (Grant number: RPG-2017-281) for funding and providing the opportunity to conduct this research.

### References

1. Charnley, J., The lubrication of animal joints in relation to surgical reconstruction by arthroplasty. *Annals of the Rheumatic Diseases*, 1960. 19(1): p. 10.
2. McCutchen, C.W., The frictional properties of animal joints. *Wear*, 1962. 5(1): p. 1-17.
3. Dowson, D. Modes of lubrication in human joints. in *Proceedings of the Institution of Mechanical Engineers, Conference Proceedings*. 1966. SAGE Publications Sage UK: London, England.
4. Mow, V.C., The role of lubrication in biomechanical joints. *Journal of Lubrication Technology*, 1969. 91(2): p. 320-326.
5. Jin, Z. and D. Dowson, Elastohydrodynamic lubrication in biological systems. *Proceedings of the Institution of Mechanical Engineers, Part J: Journal of Engineering Tribology*, 2005. 219(5): p. 367-380.
6. Ateshian, G.A., The role of interstitial fluid pressurization in articular cartilage lubrication. *Journal of Biomechanics*, 2009. 42(9): p. 1163-1176.
7. Ateshian, G.A., et al., An asymptotic solution for the contact of two biphasic cartilage layers. *Journal of Biomechanics*, 1994. 27(11): p. 1347-1360.
8. Hayes, W., et al., A mathematical analysis for indentation tests of articular cartilage. *Journal of Biomechanics*, 1972. 5(5): p. 541-551.
9. Mak, A.F., W.M. Lai, and V.C. Mow, Biphasic indentation of articular cartilage—I. Theoretical analysis. *Journal of Biomechanics*, 1987. 20(7): p. 703-714.
10. Schinagl, R.M., et al., Depth-dependent confined compression modulus of full-thickness bovine articular cartilage. *Journal of Orthopaedic Research*, 1997. 15(4): p. 499-506.
11. Chen, A., et al., Depth-and strain-dependent mechanical and electromechanical properties of full-thickness bovine articular cartilage in confined compression. *Journal of Biomechanics*, 2001. 34(1): p. 1-12.
12. Chen, X., et al., Determining tension-compression nonlinear mechanical properties of articular cartilage from indentation testing. *Annals of Biomedical Engineering*, 2016. 44(4): p. 1148-1158.
13. Arbabi, V., et al., Determination of the mechanical and physical properties of cartilage by coupling poroelastic-based finite element models of indentation with artificial neural networks. *Journal of Biomechanics*, 2016. 49(5): p. 631-7.
14. Meloni, G.R., et al., Biphasic Finite Element Modeling Reconciles Mechanical Properties of Tissue-Engineered Cartilage Constructs Across Testing Platforms. *Tissue Engineering Part A*, 2017. 23(13-14): p. 663-674.

15. Krishnan, R., M. Kopacz, and G.A. Ateshian, Experimental verification of the role of interstitial fluid pressurization in cartilage lubrication. *Journal of Orthopaedic Research*, 2004. 22(3): p. 565-570.
16. Katta, J., et al., Effect of load variation on the friction properties of articular cartilage. *Proceedings of the Institution of Mechanical Engineers, Part J: Journal of Engineering Tribology*, 2007. 221(3): p. 175-181.
17. Pawaskar, S., Z. Jin, and J. Fisher, Modelling of fluid support inside articular cartilage during sliding. *Proceedings of the Institution of Mechanical Engineers, Part J: Journal of Engineering Tribology*, 2007. 221(3): p. 165-174.
18. Reale, E.R. and A.C. Dunn, Poroelasticity-driven lubrication in hydrogel interfaces. *Soft Matter*, 2017. 13(2): p. 428-435.
19. Qiu, M., et al., Designing prosthetic knee joints with bio-inspired bearing surfaces. *Tribology International*, 2014. 77: p. 106-110.
20. Sokoloff, J., Theory of the effects of surface roughness on fluid lubrication of hydrogels. *Soft Matter*, 2012. 8(31): p. 8164-8170.
21. Moore, A.C. and D.L. Burris, Tribological rehydration of cartilage and its potential role in preserving joint health. *Osteoarthritis and Cartilage*, 2017. 25(1): p. 99-107.
22. Burris, D.L. and A.C. Moore, *Cartilage and Joint Lubrication: New Insights Into the Role of Hydrodynamics*. *Biotribology*, 2017. 12: p. 8-14.
23. Graham, B.T., et al., Sliding enhances fluid and solute transport into buried articular cartilage contacts. *Osteoarthritis and Cartilage*, 2017. 25(12): p. 2100-2107.
24. Biot, M.A., *Mechanics of Deformation and Acoustic Propagation in Porous Media*. *Journal of Applied Physics*, 1962. 33(4): p. 1482-1498.
25. Mow, V.C., et al., Biphasic creep and stress relaxation of articular cartilage in compression: theory and experiments. *Journal of Biomechanical Engineering*, 1980. 102(1): p. 73-84.
26. Simon, B.R., Multiphase poroelastic finite element models for soft tissue structures. *Applied Mechanics Reviews*, 1992. 45(6): p. 191-218.
27. Ateshian, G.A. and H. Wang, A theoretical solution for the frictionless rolling contact of cylindrical biphasic articular cartilage layers. *Journal of Biomechanics*, 1995. 28(11): p. 1341-1355.
28. Sakai, N., et al., A functional effect of the superficial mechanical properties of articular cartilage as a load bearing system in a sliding condition. *Biosurface and Biotribology*, 2016. 2(1): p. 26-39.
29. Murakami, T., et al., Importance of adaptive multimode lubrication mechanism in natural synovial joints. *Tribology International*, 2017. 113: p. 306-315.
30. Wu, J., W. Herzog, and M. Epstein, Evaluation of the finite element software ABAQUS for biomechanical modelling of biphasic tissues. *Journal of Biomechanics*, 1997. 31(2): p. 165-169.
31. Olsen, S. and A. Oloyede, A finite element analysis methodology for representing the articular cartilage functional structure. *Computer Methods in Biomechanics & Biomedical Engineering*, 2002. 5(6): p. 377-386.
32. Mattei, L., et al., Finite element analysis of the meniscectomised tibio-femoral joint: implementation of advanced articular cartilage models. *Computer Methods in Biomechanics and Biomedical Engineering*, 2014. 17(14): p. 1553-1571.
33. Li, J., et al., Biphasic investigation of contact mechanics in natural human hips during activities. *Proceedings of the Institution of Mechanical Engineers, Part H: Journal of Engineering in Medicine*, 2014. 228(6): p. 556-563.
34. Maas, S.A., et al., FEBio: finite elements for biomechanics. *Journal of Biomechanical Engineering*, 2012. 134(1): p. 011005.
35. Smyth, P.A. and I. Green, Analysis of Coupled Poroelastocoelectricity and Hydrodynamic Lubrication. *Tribology Letters*, 2017. 65(1): p. 1.
36. de Boer, G., et al., An investigation into the contact between soft elastic and poroelastic bodies rotating under load. *Tribology-Materials, Surfaces & Interfaces*, 2017: p. 1-9.
37. Bower, A., The influence of crack face friction and trapped fluid on surface initiated rolling contact fatigue cracks. *Journal of Tribology*, 1988. 110(4): p. 704-711.
38. Balcombe, R., et al., A coupled approach for rolling fatigue cracks in the hydrodynamic regime: The importance of fluid/solid interactions. *Wear*, 2011. 271(5-6): p. 720-733.
39. Dallago, M., et al., The role of lubricating pressurization and entrapment on the path of inclined edge cracks originated under rolling-sliding contact fatigue: Numerical analyses vs. experimental evidences. *International Journal of Fatigue*, 2016. 92(2): p. 517-530.
40. Klein, J., Hydration lubrication. *Friction*, 2013. 1(1): p. 1-23.
41. Selvadurai, A. and A. Suvorov, Coupled hydro-mechanical effects in a poro-hyperelastic material. *Journal of the Mechanics and Physics of Solids*, 2016. 91: p. 311-333.

42. Selvadurai, A. and A. Suvorov, On the inflation of poro-hyperelastic annuli. *Journal of the Mechanics and Physics of Solids*, 2017. 107: p. 229-252.
43. Greenwood, J. and J. Tripp, The contact of two nominally flat rough surfaces. *Proceedings of the institution of Mechanical Engineers*, 1970. 185(1): p. 625-633.
44. Johnson, K., J. Greenwood, and S. Poon, A simple theory of asperity contact in elastohydro-dynamic lubrication. *Wear*, 1972. 19(1): p. 91-108.
45. Liu, Q., et al., Friction in highly loaded mixed lubricated point contacts. *Tribology Transactions*, 2009. 52(3): p. 360-369.
46. Lizhang, J., et al., The effect of contact stress on cartilage friction, deformation and wear. *Proceedings of the Institution of Mechanical Engineers, Part H: Journal of Engineering in Medicine*, 2011. 225(5): p. 461-475.
47. Gao, L., D. Dowson, and R.W. Hewson, A numerical study of non-Newtonian transient elastohydrodynamic lubrication of metal-on-metal hip prostheses. *Tribology International*, 2016. 93: p. 486-494.
48. Bonnevie, E., et al., Elastoviscous Transitions of Articular Cartilage Reveal a Mechanism of Synergy between Lubricin and Hyaluronic Acid. *PLOS One*, 2015.
49. Moore, A.C., et al., A review of methods to study hydration effects on cartilage friction. *Tribology-Materials, Surfaces & Interfaces*, 2017. 11(4): p. 202-214.
50. Erne, O.K., et al., Depth-dependent strain of patellofemoral articular cartilage in unconfined compression. *Journal of Biomechanics*, 2005. 38(4): p. 667-672.
51. Whitaker, S., Flow in porous media I: A theoretical derivation of Darcy's law. *Transport in Porous Media*, 1986. 1(1): p. 3-25.
52. Dowson, D., A generalized Reynolds equation for fluid-film lubrication. *International Journal of Mechanical Sciences*, 1962. 4(2): p. 159-170.
53. Forster, H. and J. Fisher, The influence of loading time and lubricant on the friction of articular cartilage. *Proceedings of the Institution of Mechanical Engineers, Part H: Journal of Engineering in Medicine*, 1996. 210(2): p. 109-119.
54. Caligaris, M. and G.A. Ateshian, Effects of sustained interstitial fluid pressurization under migrating contact area, and boundary lubrication by synovial fluid, on cartilage friction. *Osteoarthritis and Cartilage*, 2008. 16(10): p. 1220-1227.
55. Bonnevie, E., et al., Fluid load support during localized indentation of cartilage with a spherical probe. *Journal of Biomechanics*, 2012. 45(6): p. 1036-1041.

## Appendix A

In order to establish a validation of the porohyperelastic lubrication model a study was conducted to compare results with experiments established in the literature. To do this a variation of the operating conditions used in the main body of this article was implemented. This allowed solutions to be comparable with previous studies, whereas the results presented in the main body provide an investigation into representative conditions for the problem geometry and material in operation. As such, in this section the cartilage body does not rotate  $\Omega_0 = 0$  and instead the rigid impermeable surface translates in the horizontal direction with speed  $U$ . In turn this implies that the source term of the fluid flow governing equation (Eq. (5)) is zero and the sliding speed at the contacting interface in the lubricating flux equation (Eq. (8)) is maintained to be  $U = 0.1$  m/s as specified for the steady-state case. All other operational conditions and material properties remain the same as presented for the steady-state case described in the main body.

The solution procedure described in Section 2.3.2 required a change in order to account for numerical relaxation of the axial speed  $\Omega_0$ , where in Step 2 solutions were found to be very sensitive to the axial speed approaching zero. Hence an arbitrary small value of  $\Omega_0 = 0.01$  rad/s was specified for Steps 1 and 2, subsequently in Step 3 this was linearly reduced to zero over the solution time. This variation converged in a time period much smaller than the time period over which the load balance was considered. Results generated by this procedure are therefore at the same load and speed as presented for the steady-state case in Section 3.2.1 of the main body but where the cartilage does not rotate and instead the rigid impermeable surface slides at the same interfacial sliding speed  $U$ .

In Figure A1 and Figure A2 the distributions of von Mises' stress in solid phase and pressure in the fluid phase of the cartilage material are respectively given for this case. Additionally, Figure A3a provides the solution to the contact pressure, lubricating pressure and film thickness at the contacting interface, with Figure A3b showing the lubricating flux and flow into and out of the cartilage material at this boundary. Some notable differences to the corresponding results given in Section 3.2.1 are observed, where for example in this case the solid phase carries  $L_s = 1390$  N/m and the fluid only  $L_f = 110$  N/m. This results in a significantly larger solid



stress and significantly lower fluid pressure than in the case where the cartilage rotates and the rigid surface is stationary. Figure A1 and Figure A2 clearly show this difference in comparison to Figure 4 and Figure 5 respectively, with the addition that the contact area is much larger in this case.

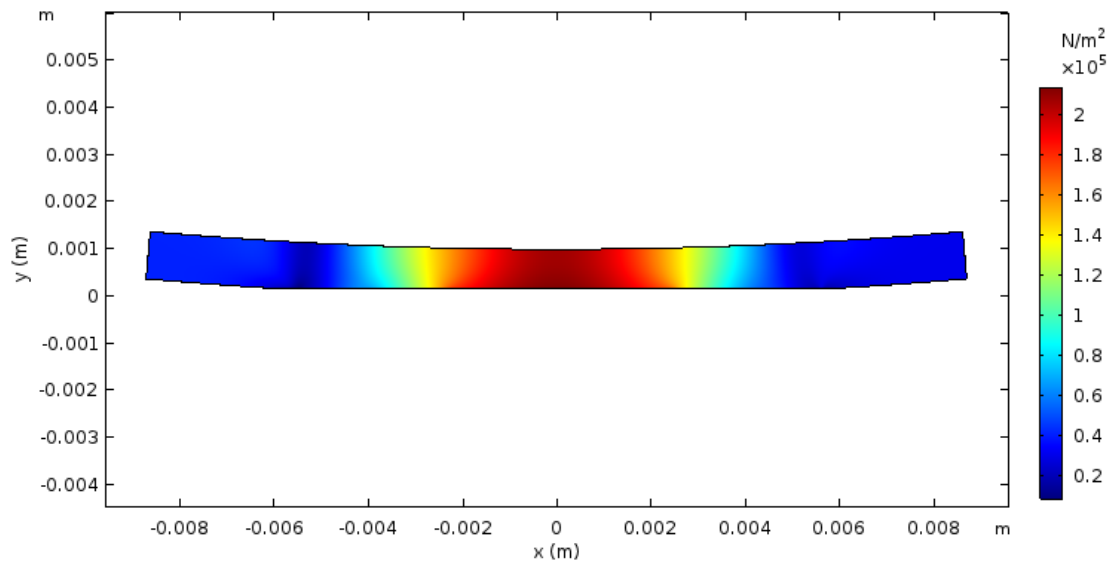


Figure A1 – Distribution of von Mises' stress in the solid phase where the cartilage is stationary and the rigid impermeable surface slides (steady-state solution).

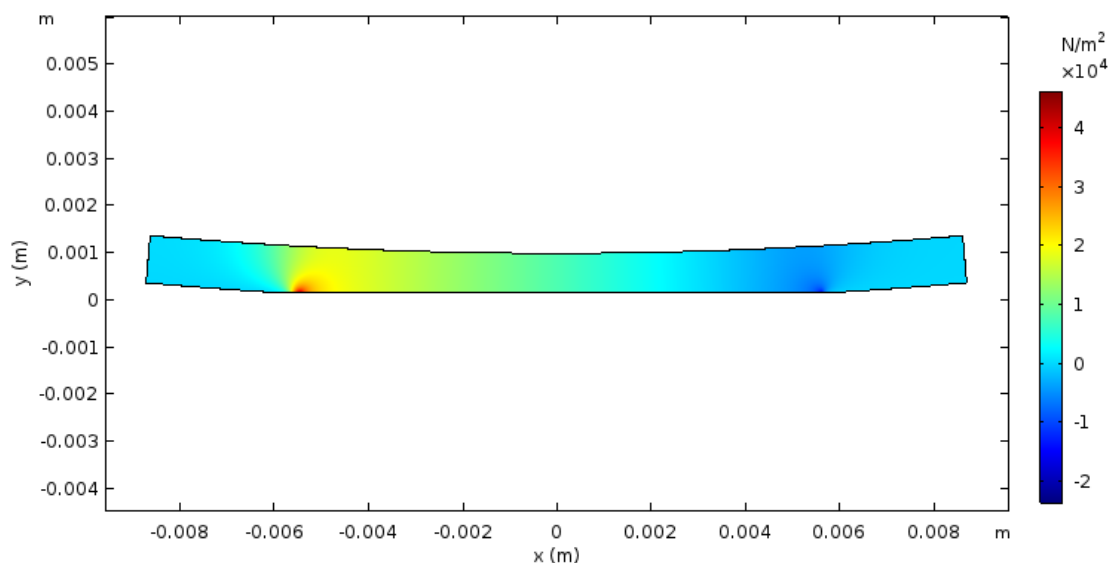


Figure A2 – Distribution of pressure in the fluid phase where the cartilage is stationary and the rigid impermeable surface slides (steady-state solution).

The contact stress and film thickness in Figure A3a represent similar distributions to that of Figure 6a, whereas in this case the pressure is only increasing at the inlet of the contact region and then decreases to a minimum at the outlet of the contact region. This relates to the lack of any source term in the fluid flow governing equation caused by rotation of the cartilage material into and out of the contacting interface, here pressure is only generated as a result of the sliding interface in the thin film lubrication which diminishes to zero when the film thickness is negligible. Corresponding to this Figure A3b shows a similarities and differences with Figure 6b. In both cases fluid in the lubricating region before the inlet of the contact is positive which provides a flow into the cartilage material, however in this case there is an additional flow out of the material upstream of this to support this flow. For this case in the contact region there is no flow and then at the outlet flow enters the cartilage material providing a positive lubricating flux in this region, upstream of this fluid moves out of the cartilage material to support this. This differs to the rotating cartilage case where flow into the material was observed in the outlet

region providing a negative lubricating flux, subsequently followed by a flow out of the material supporting a positive lubricating flux downstream.

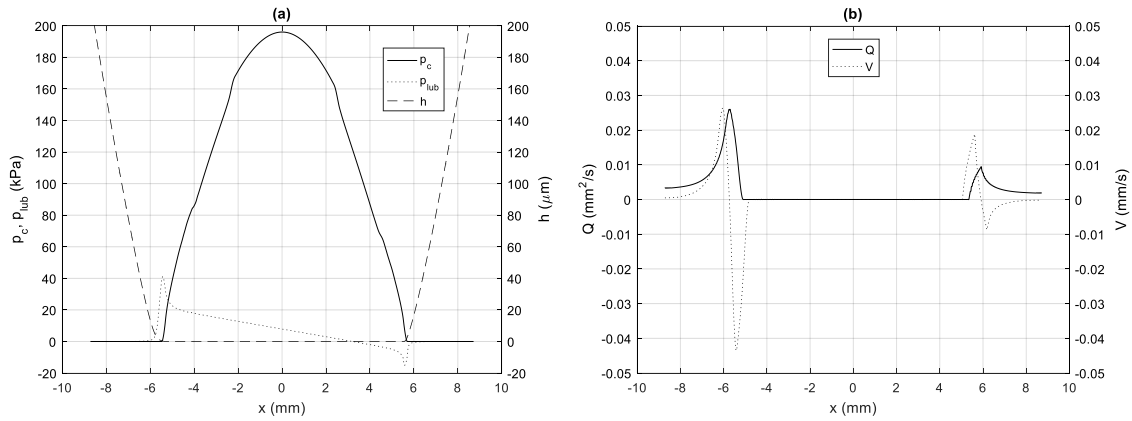


Figure A3 – Steady-state solution for the contacting interface AB where the cartilage is stationary and the rigid impermeable surface slides. Showing distributions of: (a) the contact stress,  $p_c$ , pressure,  $p_{lub}$ , and film thickness  $h$ ; and (b) the lubricating flux in the thin film,  $Q$ , and flow at the porohyperelastic surface,  $V = \mathbf{q} \cdot \mathbf{x}_n$ , where a positive sign indicates flow out of the rotating body.